Monthly Notices
of the
ROYAL ASTRONOMICAL SOCIETY

MNRAS **464,** 2139–2173 (2017)
Advance Access publication 2016 September 30

doi:10.1093/mnras/stw2477

Probing the active galactic nucleus unified model torus properties in Seyfert galaxies

Anelise Audibert,[1]★ Rogério Riffel,[1]★ Dinalva A. Sales,[2] Miriani G. Pastoriza[1] and Daniel Ruschel-Dutra[1]

[1]*Departamento de Astronomia, Universidade Federal do Rio Grande do Sul, 9500 Bento Gonçalves, Porto Alegre 91501-970, Brazil*
[2]*Instituto de Matemática, Estatística e Física, Universidade Federal do Rio Grande, Rio Grande 96203-900, Brazil*

Accepted 2016 September 28. Received 2016 September 27; in original form 2016 January 8

ABSTRACT

We studied the physical parameters of a sample comprising of *all Spitzer*/Infrared Spectrograph public spectra of Seyfert galaxies in the mid-infrared (5.2–38 μm range) under the active galactic nucleus (AGN) unified model. We compare the observed spectra with $\sim 10^6$ CLUMPY model spectral energy distributions, which consider a torus composed of dusty clouds. We find a slight difference in the distribution of line-of-sight inclination angle, i, requiring larger angles for Seyfert 2 (Sy 2) and a broader distribution for Seyfert 1 (Sy 1). We found small differences in the torus angular width, σ, indicating that Sy 1 may host a slightly narrower torus than Sy 2. The torus thickness, together with the bolometric luminosities derived, suggests a very compact torus up to ∼6 pc from the central AGN. The number of clouds along the equatorial plane, N, as well the index of the radial profile, q, is nearly the same for both types. These results imply that the torus cloud distribution is nearly the same for type 1 and type 2 objects. The torus mass is almost the same for both types of activity, with values in the range of $M_{\rm tor} \sim 10^4 - 10^7\,{\rm M}_\odot$. The main difference appears to be related to the clouds' intrinsic properties: type 2 sources present higher optical depths τ_V. The results presented here reinforce the suggestion that the classification of a galaxy may also depend on the intrinsic properties of the torus clouds rather than simply on their inclination. This is in contradiction with the simple geometric idea of the unification model.

Key words: molecular processes – galaxies: active – galaxies: nuclei – galaxies: Seyfert – infrared: galaxies.

1 INTRODUCTION

According to the unified model, the energy from active galactic nuclei (AGNs) is powered by the accretion of matter into a supermassive black hole (Lynden-Bell 1969; Begelman, Blandford & Rees 1984). The unification scheme suggests that the different AGN types are explained by the line-of-sight (LOS) orientation of an obscuring material, which surrounds the central source and is arranged in an axisymmetric/toroidal geometry and composed primarily of gas and dust. Under edge-on views, it obscures the radiation from the accretion disc and broad-line region (BLR). Such an object is classified as a type 2 AGN. When viewed face-on, the central engine can be observed directly. These galaxies are classified as type 1 AGNs (Antonucci 1993; Urry & Padovani 1995). The unified model was first supported through spectropolarimetric observations of the Seyfert 2 (Sy 2) galaxy NGC 1068 (Antonucci & Miller 1985), revealing the polarized broad emission lines, and followed by other polarized broad-line observations in type 2 AGNs (e.g. Tran, Miller & Kay 1992; Tran 1995). This hidden type 1 emission can be visible via light scattering in the ionizing cones, which corresponds to ionizing radiation that is collimated by the torus opening angle, providing additional indirect evidence for the unified model (e.g. Pogge 1988; Storchi-Bergmann & Bonatto 1991; Storchi-Bergmann, Wilson & Baldwin 1992).

The dusty structure of the AGN unified model is responsible for absorbing short-wavelength light from the active nucleus and re-emitting it mainly in the infrared (IR) wavelengths, leading to a peculiar signature in the spectral energy distribution (SED) of a galaxy. In specific, the silicate feature at 9.7 μm in the mid-infrared (MIR) is frequently found in absorption in type 2 and is also expected to appear in emission in type 1. However, in most type 1 objects, this feature is either mild or absent (Hao et al. 2007; Wu et al. 2009). In addition, there are some cases where silicate emission is detected in type 2 (e.g. in Sy 2 NGC 2110 by Sturm et al. 2006; Mason et al. 2009). Consequently, the MIR spectral range hosts fundamental features necessary to study the putative torus required in the unified model for AGNs. The recent significant

★ E-mail: anelise.audibert@obspm.fr (AA); riffel@ufrgs.br (RR)

advances in observational facilities, such as Atacama Large Millimeter/submillimeter Array (ALMA) and Very Large Telescope Interferometer (VLTI), now allow us to resolve the central parsec scales in nearby AGNs. So far, only a few VLTI observations achieve sufficient spatial resolution to isolate the emission of these obscured structures. For instance, the cases of NGC 1068 (Jaffe et al. 2004; López-Gonzaga et al. 2014; Gratadour et al. 2015) and Circinus (Tristram et al. 2007, 2014). Very recently, García-Burillo et al. (2016) and Imanishi, Nakanishi & Izumi (2016) presented the first resolved images of the torus of NGC 1068, the former using the continuum and the CO(6–5) emission observed with ALMA band 9 and the latter using HCN(3–2) and HCO^+(3–2) emission lines. These cases are successful precedents for forthcoming ALMA observations intended to study molecular gas in the torus and its surrounding (Netzer 2015). While there are no plenty of data with such detailed observations, the optimal way to probe the physical processes related to the torus is understanding the radiation reprocessing mechanisms responsible for the singular behaviour of the AGN SEDs.

In the last two decades, several models have been developed in order to understand the torus emission. For example, Krolik & Begelman (1988) proposed that the torus should constitute of a large number of optically thick dusty clouds, otherwise the dust grains would be destroyed by the high AGN energy luminosity. Their presumption is reinforced by VLTI interferometric observations in the *N*-band range (8–13 μm) performed by Tristram et al. (2007) in the nucleus of the Circinus galaxy, providing strong evidence of a clumpy and dusty structure. Due to computational issues in modelling a clumpy medium, some studies have explored the effect of a dusty uniform distribution in a toroidal geometry (Pier & Krolik 1992; Granato & Danese 1994; Efstathiou & Rowan-Robinson 1995; Dullemond & van Bemmel 2005; Fritz, Franceschini & Hatziminaoglou 2006). However, to explain the low-resolution (>1 arcsec) observed SEDs and IR spectra in such homogeneous descriptions, the models force the torus size to be at scales of $\gtrsim$100 pc. With the advent of high spatial resolution using 8 m class telescopes, it was demonstrated that the surrounded dusty environment is much more compact, with sizes of a few parsecs (Jaffe et al. 2004; Burtscher et al. 2009; Tristram et al. 2009).

Nevertheless, in the last few years, some efforts have been made to handle a clumpy formalism and they can naturally explain the problem with the silicate issue mentioned above (Nenkova, Ivezić & Elitzur 2002; Hönig et al. 2006; Nenkova et al. 2008a,b; Schartmann et al. 2008; Stalevski et al. 2012). Among them, the CLUMPY models presented by Nenkova et al. (2002, 2008a,b) are, to date, some of the most successful models for representing the re-processed MIR torus emission and allowing us to constrain some torus properties. They consist of a large data base of theoretical SEDs resulting from a 1D radiative transfer code (DUSTY; Ivezic, Nenkova & Elitzur 1999) taking into account the continuum emission from clumpy media with shadowed individual clouds. One of the advantages of a clumpiness formalism is that they can reproduce more realistic MIR spectra. This is because they have a wide range of dusty cloud temperatures at the same radius from the central source and even distant clouds can be directly illuminated by the AGN, contrary to the smooth density distributions. The CLUMPY models have been used by several works to study the torus properties, for example, in a X-ray selected sample of AGNs by Mateos et al. (2016), in a sample of 26 quasars by Mor, Netzer & Elitzur (2009), in an analysis of 27 Sy 2 by Lira et al. (2013) and in modest to small samples of Seyfert galaxies (e.g. Ichikawa et al. 2015) and the works from Alonso-Herrero et al. (2011) and Ramos Almeida et al. (2009, 2011), hereafter AH11, RA09 and RA11, respectively. One of the main differences between our work and AH11 and RA11 is the use of near-infrared (NIR) data for all the galaxies in their analysis and our much larger sample.

We investigated the torus properties of 111 Seyfert galaxies using data archive from Infrared Spectrograph (IRS; Houck et al. 2004) aboard the *Spitzer Space Telescope* in the 5.2–38 μm spectral range. We compared the sample with the CLUMPY theoretical SEDs from Nenkova et al. (2002, 2008a,b) using two different approaches: the $\chi^2_{\rm red}$ test and Bayesian inference (BayesCLUMPY; Asensio Ramos & Ramos Almeida 2009). Section 2 characterizes the sample and data reduction. In Section 3, we describe the CLUMPY models, the polycyclic aromatic hydrocarbon (PAH) decontamination from the SEDs and the different approaches utilized to fit the data. The main results and the discussion are summarized in Section 4, and the contribution of the NIR data is exploited in Section 5. Our conclusions are presented in Section 6.

2 THE DATA

We have performed an analysis on a sample of 111 nearby galaxies classified as Seyfert galaxies that were available in the *Spitzer* Heritage Archive. The sample consists of 84 galaxies that have been presented in previous works (Wu et al. 2009; Gallimore et al. 2010), 14 galaxies from Sales, Pastoriza & Riffel (2010) and another 13 objects available in the *Spitzer* archive (presented here for the first time). The galaxies were observed with the IRS using two low spectral resolution ($R \sim 60$–127) modules: short-low (SL) and long-low (LL), covering a wavelength range from 5.2 to 38 μm in the MIR. The SL module has an image scale of 1.8 arcsec pixel^{-1} and the LL module 5.1 arcsec pixel^{-1}. Both are sub-divided in orders 1 and 2.

With the exception of seven galaxies whose spectra are available from the SINGS Legacy programme[1] (PID 159; Kennicutt et al. 2003), all other data were processed using the Basic Calibration Data (BCD) pipeline[2] (version 18.18). The BCD pipeline manages the raw data through basic processing, such as the detection of cosmic rays, the removal of saturated pixels, dark current and flat-field subtraction and droop correction. For the sample presented in Gallimore et al. (2010), 78 objects have the spectral mapping mode available, while the other 6 present the mapping mode only in LL and SL observations in the staring mode (NGC 526A, NGC 4941, NGC 3227, IC 5063, NGC 7172 and NGC 7314).

The mapping mode observations were processed by employing the CUbe Builder for IRS Spectra Maps (CUBISM; Smith et al. 2007a) to construct the data cubes. Sky subtraction was evaluated from an average spectra of the off-source orders, e.g. while the source is centred in the first order, the second order is pointed at the sky in an offset position. We used a 3.9 × 11.1 pixel extraction (equivalent to a 10 arcsec circular radius aperture centred on the brightest source) to extract the spectra. In a few cases, the extractions showed a mismatch between the modules or their orders that was corrected by scaling the spectra as recommended by Smith et al. (2007b).

For the remaining 27 objects, the data are available in staring mode and the calibrated spectra were obtained from the Cornell Atlas of *Spitzer*/IRS Sources (CASSIS; Lebouteiller et al. 2011). CASSIS[3] provides optimal extractions and diagnostic tools to

[1] The IRS data from the SINGS Legacy Project are available at http://irsa.ipac.caltech.edu/data/SPITZER/SINGS/. The nuclear spectra were extracted over a 50 arcsec × 33 arcsec aperture.
[2] For more details, please see the IRS Instrument Handbook.
[3] CASSIS products are available at http://cassis.astro.cornell.edu/atlas

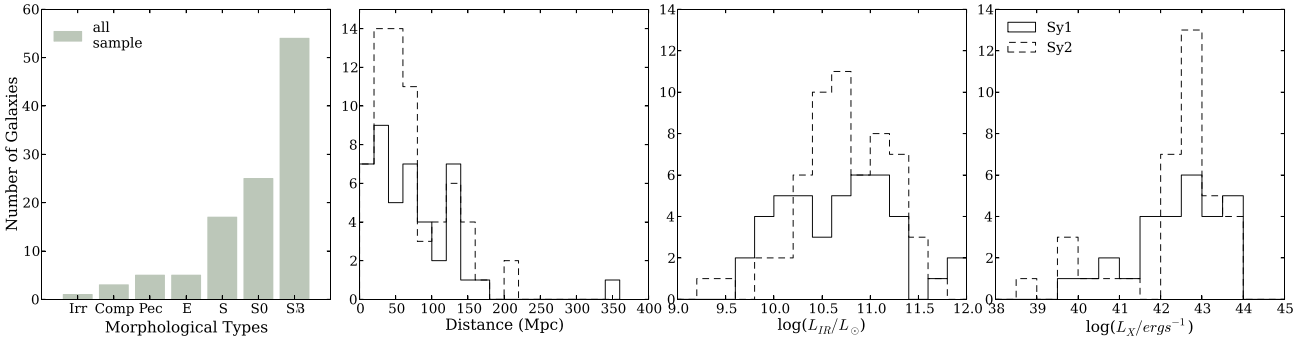

Figure 1. Characteristics of the 111 AGN samples. The solid line histograms show the properties for Sy 1 galaxies while the dashed lines represent the Sy 2 sources. Morphological classification and distances were obtained from the NED – NASA/IPAC Extragalactic Database or from Whittle (1992). In the left-hand panel, we gathered all morphological types into seven mean classes: irregular (Irr), compact (Comp), peculiar (Pec), elliptical (E), spiral (S), lenticular (S0) and barred spiral (SB). The references for $L_{\rm IR}$ and $L_{\rm X}$ can be found in Table A1.

guarantee the most accurate background subtraction, especially for faint sources. In most cases, the optimal CASSIS extraction pointed to sky subtraction through the off-order method. However, in a few cases, CASSIS indicated the subtraction by nod positions as the best spectral extraction. Furthermore, the majority of CASSIS products were established as point-like sources.[4]

Our final sample is composed of 45 Sy 1 and 65 Sy 2 galaxies with redshifts between $0.002 \leq z \leq 0.079$. The AGNs are preferentially found in host galaxies with barred spiral, lenticulars or in spiral morphological types. The mean values for the IR luminosities are $L_{\rm IR}({\rm Sy\ 1}) = 4.64 \times 10^{10}\,{\rm L}_{\odot}$ for Sy 1 and $L_{\rm IR}({\rm Sy\ 2}) = 5.44 \times 10^{10}\,{\rm L}_{\odot}$ for Sy 2 and for the hard X-ray luminosities are $L_{2-10\,{\rm keV}}({\rm Sy\ 1}) = 1.59 \times 10^{43}$ for Sy 1 and $L_{2-10\,{\rm keV}}({\rm Sy\ 2}) = 1.19 \times 10^{43}$ erg s^{-1} for Sy 2. The sample properties are summarized in Fig. 1 and listed in Table A1.

2.1 Removing the PAH contamination

Since the IRS *Spitzer* spectra were extracted in a 20 arcsec circular diameter aperture, corresponding to ∼1–20 kpc of the galaxies (except for $z = 0.79$, Mrk 478 that represents ∼33 kpc), the host galaxy contribution is unavoidable in our sample. In order to minimize the effects from star formation and to isolate the AGN emission of the galaxy, we have adopted a similar method as that used in Lira et al. (2013). They remove the stellar contribution by subtracting templates developed by Smith et al. (2007b), when the MIR is dominated by PAH emission of star-forming regions.

Instead of fitting star formation templates, we chose to follow another approach in order to attenuate the PAH's contribution (and therefore, that of the host galaxy) in the spectra. We applied the PAHFIT tool developed by Smith et al. (2007b). This code decomposes the emission lines of the low-resolution IRS *Spitzer* spectra, modelling them as the sum of starlight continuum, thermal dust continuum and emission lines (pure rotational lines of H_2, fine structure lines and dust emission features). All flux intensity components are affected by dust extinction, quantified by the optical depth (for more details, see Smith et al. 2007b).

Since the continuum from our Seyfert sample is not only due to dust and stellar components, but also due to the AGN power-law continuum, we decided to subtract only the emission lines from the H_2 and the molecular features of PAH emission from the observed spectra. It is, however, worth mentioning that most of the PAH contribution lies in 5–15 μm, where the stellar emission is more prominent. For longer wavelengths, the host galaxy emission is very difficult to distinguish from the AGN continuum, and unfortunately, the current spectral decomposition codes are unable to separate each contribution for $\lambda \gtrsim 20$ μm (e.g. Smith et al. 2007b; Hernán-Caballero et al. 2015). This trend might overestimate AGN emission at longer wavelengths, which could bias the outputs of the CLUMPY models towards extended and broader tori, due to the cooler dust that peaks in the far-infrared (far-IR) range. None the less, recently Fuller et al. (2016) separated the AGN and PAH components using the full wavelength coverage of the *Spitzer*/IRS spectra of 11 Seyfert galaxies. They used the templates provided by Hernán-Caballero et al. (2015) and then compared the AGN resulting spectra with the 31.5 μm imaging photometry from the Stratospheric Observatory For Infrared Astronomy (SOFIA), finding that most of the sources are AGN dominated at 31.5 μm.

In Fig. 2, we present some representative examples of this approach.[5] Shown is a case with strong PAH emission and second with little PAH feature contribution (Sy 1 NCG 1365 and Sy 2 NGC 1275, respectively). Also, we selected an example of deep silicate absorption in 9.7 μm for NGC 7172, which is surrounded by PAH emission. As can be seen, the effect of the molecular emission features is more prominent at shorter wavelengths and can alter the shape of the spectrum. The majority of galaxies (about 80 per cent of the sample) exhibit a substantial star-forming contribution (see also Sales et al. 2010).

Recently, some other studies have been supporting this star-forming subtraction methodology. For instance, in Ruschel-Dutra et al. (2014), there is no PAH emission detected using high-resolution nuclear spectra from T-ReCs when compared with IRS observations of NGC 7213 and NGC 1386. Also, no PAH emission bands were detected in the nuclear region (∼200 pc) of Mrk 3, a Compton-thick Sy 2, using Michelle/Gemini spectrograph (Sales et al. 2014). Davies et al. (2012) argued that the PAH molecules cannot survive in a radius smaller than 50 pc, a value corresponding to a region larger than that of the torus extension (parsec scale; Tran et al. 1992). However, in some cases, e.g. in T-ReCs observations of NGC1808, the aromatic component was detected at 8.6 and

[4] The optimal CASSIS extractions equivalent to extended sources are Mrk 471, Mrk 609, Mrk 993, NGC 5695, NGC 5782, NGC 7679 and NGC 7682.

[5] In Appendix B, we present the adjustments for all the objects in the sample. The decomposed spectra files are available upon request, please contact the authors.

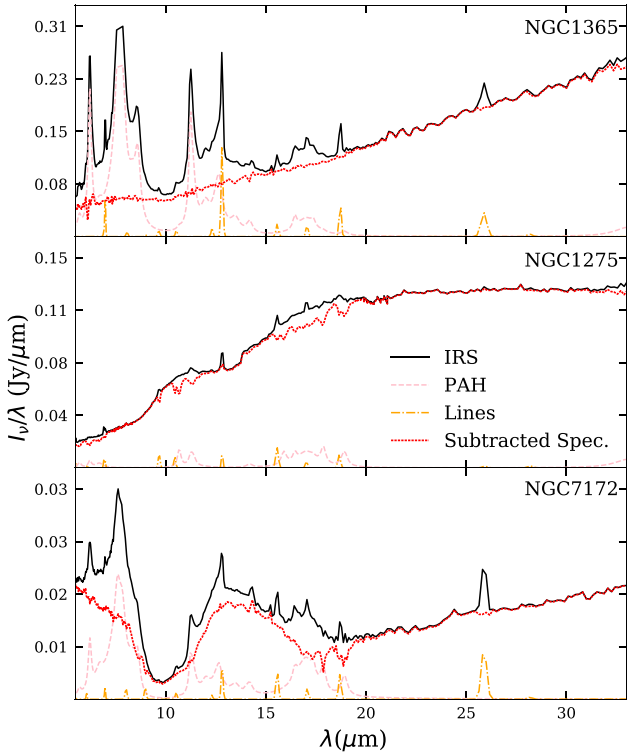

Figure 2. Typical examples of the subtraction of the PAH and ionic line components from the spectra. The black lines represent the observed spectra, while the dot–dashed orange and dashed pink lines show the resulting adjusted spectra created by fitting the PAH emission and ionic and hydrogen lines, respectively, using the PAHFIT tool. The dotted red lines show the subtracted spectra that were handled in our analysis. In the top panel, the results for NGC 1365 are shown, characterizing a galaxy with strong PAH emission. On the other hand, the middle panel shows little contribution from this feature for NGC 1275. An example of a deep silicate absorption and PAH emission is presented in the bottom panel for the Sy 2 NGC 7172.

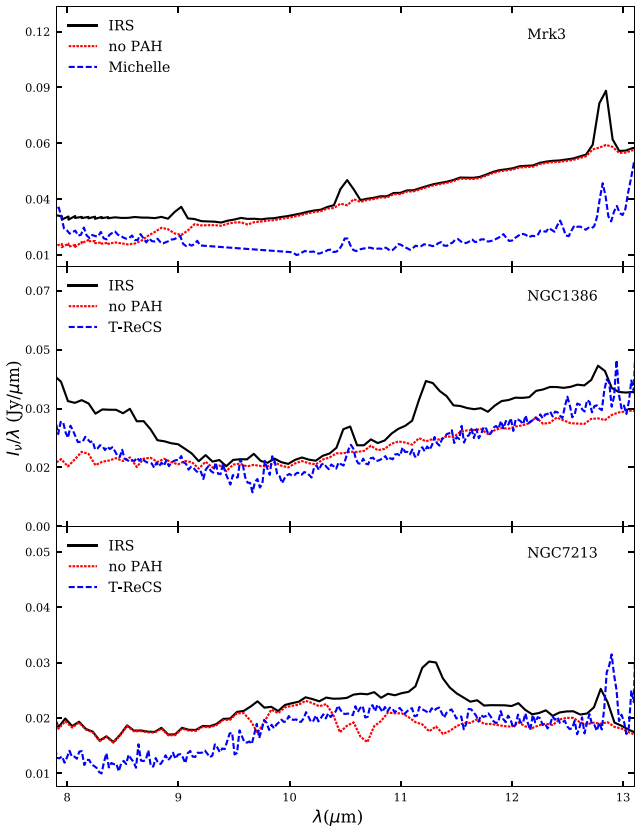

Figure 3. We show a comparison of the low-resolution *Spitzer* IRS spectra and the ground-based nuclear emission observations. The top panel shows the spectrum of Mrk 3 from Michelle while the middle and bottom panels show the data from T-ReCs for NGC 1386 and NGC 7213, respectively. The black lines represent the IRS data, the dotted red lines the starburst subtracted spectra and the dashed blue lines the high-resolution spectra. Except in the case of Mrk 3, the subtracted spectra appear to well represent the emission from the active nucleus.

11.3 μm in the galaxy centre (∼26 pc) up to a radius of 70 pc from the nucleus (Sales et al. 2013).

To illustrate the effect of the starburst subtraction method, we show in Fig. 3 the high-resolution data from Michelle and T-ReCs of the galaxies Mrk 3, NGC 1386 and NGC 7213, compared to the IRS spectra. Also shown are the final spectra resulting from the subtraction of the PAH components. The clean IRS spectra tend to better approximate the nuclear spectra from high-resolution observations except for the Mrk 3. This is possibly due to the fact that this galaxy is a Compton-thick object and has a heavy absorbed dust/gas component ($N_H \sim 1.1 \times 10^{24}$ cm^{-2}; Sales et al. 2014) obscuring the nucleus, leading to a higher continuum in the *Spitzer* observation. Moreover, the fact that this galaxy has a small starburst contribution may explain why we see almost no differences between the IRS spectra and the subtracted one. However, in the cases of NGC 1386 and NGC 7213, we believe that the PAH subtraction approach represents a good approximation of the nuclear emission. Thus, the spectral decomposition methodology was applied to all the objects used in our study.

3 MODELLING THE SED IN THE MIR

3.1 CLUMPY torus models

A clumpy medium provides a natural explanation for the silicate absorption feature that was expected to be observed in emission in type 1 sources but is frequently mild or even flat since it requires at least a clump obscuring the radiation at the observer's LOS.

The most successful and up-to-date clumpy models are those of the Kentucky group. Nenkova et al. (2002, 2008a,b) developed a formalism to handle a clumpy medium, considering point-like dusty clouds distributed in a toroidal geometry around the central AGN. The CLUMPY models are a large data base (∼10^6) of theoretical SEDs resulting from the radiative transfer treatment through the DUSTY code (Ivezic et al. 1999). The dust grains follow the MNR size distribution (Mathis, Rumpl & Nordsieck 1977) and are composed of the standard Galactic mixture of 47 per cent graphite with optical constants and 53 per cent cold silicates. While the graphite grains are responsible for the IR emission at $\lambda \gtrsim 1$ μm, the 9.7 and 18 μm emission and absorption features are attributed to silicate grains (e.g. Barvainis 1987; Pier & Krolik 1992; Granato & Danese 1994; Siebenmorgen, Krügel & Spoon 2004).

The CLUMPY models assume that the torus is formed by dusty clumps constrained by the following parameters: (i) the number of clouds, N_0, in the torus equatorial radius; (ii) τ_V, the optical depth of each cloud defined at 0.55 μm band; (iii) the radial extension of the clumpy distribution, $Y = R_o/R_d$, where R_o and R_d are the outer and inner radii of the torus, respectively; (iv) the radial distribution of clouds as described by a power law r^{-q}; (v) the torus angular width, σ, constrained by a Gaussian angular distribution width; and

Table 1. Parameter values adopted in fitting.

	Sampled values	Description
	CLUMPY models	
i	0–90 steps of 10°	Observer's viewing angle
N	1–15 steps of 1	Clouds along the equatorial plane
q	0–3 steps of 0.5	Power-law index of the radial distribution
τ_V	5,10,20,30,40,60,80,100,150	Optical depth of individual clouds
σ	15–70 steps of 5	Torus angular width
Y	5, 10–100 steps of 10	Torus thickness

(vi) the observer's viewing angle i. The grid of these model parameters is listed in Table 1.

The model geometry also allows us to determine other parameters that are crucial to understand the obscuration effects of the central source. They represent the number of clouds along the LOS, N_{los}, described by almost a Gaussian distribution along the equatorial plane (N), which depends on the inclination, $\beta = \pi/2 - i$, and angular width, σ, parameters

$$N_{los}(\beta) = N \exp^{-\left(\frac{\beta}{\sigma}\right)^2} \quad (1)$$

and the total optical depth of the torus along the LOS, product of the number of clouds and the optical depth of each cloud or the visual extinction

$$A_V = 1.086 N_{los} \tau_V. \quad (2)$$

One of the characteristics of Nenkova et al. models is that the SEDs reproduced are not exclusively sensitive to the inclination angle, as established by the only orientation-dependent unification schemes. The continuum shape and behaviour of the silicate features also have a strong dependence on the optical properties, characterized by the optical depth τ_V, and the number of clouds along radial rays, specifically at the equatorial plane, N. In the latter, N must be sufficiently large, $N \sim 5$–10, to ensure the attenuation of X-rays in type 2 sources while the former one was constrained to values $\tau_V \gtrsim 60$ to ensure the probability of photon escape. The explanation for many problems faced by the smoothly distribution handling is given by the clumpiness nature of the toroidal structure and, therefore, the CLUMPY models constitute a powerful tool to probe the torus physical properties proposed by the AGN's unified model.

3.2 Fitting procedure

Once we applied the procedure to isolate the nuclear emission, we performed two different approaches to compare the MIR resulting spectra from IRS observations with Nenkova's theoretical models. In the following sections, we describe the techniques employed.

3.2.1 χ^2_{red} test

We developed a code to compare each spectrum with all 10^6 CLUMPY model SEDs. The routine searches for the parameters that minimize the equation

$$^2\chi^2_{red} = \frac{1}{N} \sum_{i=1}^{N} \left(\frac{F_{obs,\lambda_i} - F_{mod,\lambda_i}}{\sigma_{\lambda_i}} \right)^2, \quad (3)$$

where N is the number of data points in the spectrum, F_{obs,λ_i} and F_{mod,λ_i} are the observed and theoretical fluxes at each wavelength and σ_{λ_i} are the uncertainties in F_{obs,λ_i}. Both F_{obs,λ_i} and F_{mod,λ_i} were normalized to unit at 28.0 μm for all the galaxies in the sample, with the uncertainties correctly propagated. The 'decontaminated' nuclear spectrum was compared to the CLUMPY theoretical SEDs, and we test the results for the best fit, e.g. the minimum χ^2_{red} and 5, 10, 15 and 20 per cent its deviation fractions, using a similar approach of Nikutta, Elitzur & Lacy (2009) and Sales et al. (2013). In this work, we choose to represent the best fit and 10 per cent of deviation solutions.

3.2.2 BayesCLUMPY technique

We apply the Bayesian inference tool BayesCLUMPY (Asensio Ramos & Ramos Almeida 2009) in order to achieve the best-fitting parameters for the observed nuclear SEDs. The technique consists to perform a Markov chain Monte Carlo method to investigate the parameter space defined by the first 13 eigenvectors. These values result from the combination of the principal component analysis and the artificial neural network that provides an interpolation in the data base of the model grid from the theoretical CLUMPY models ($\sim 10^6$ models). This approach allows us to obtain the marginal posterior distribution for each model parameter taking into account all a priori constraints and the information from the observations. To ensure the stability of the solution, we performed consecutive runs of the algorithm. It is important to emphasize that fitting CLUMPY torus models to the spectra is an intrinsically degenerate problem as we can obtain the same observable effect for different sets of parameters.

3.2.3 Final fitting

An example of fitting for some galaxies is presented in Fig. 4, and the individual fittings are presented in Appendix C. The yellow dashed line shows the model fitted for the minor χ^2_{red} value, e.g. the best fit, and the blue dot–dashed line represents the corresponding best χ^2 solution for BayesCLUMPY inference, the maximum a posteriori (MAP) values. The derived mean parameters for both χ^2_{red} and the Bayesian method are very similar, and in general the χ^2_{red} solution is the most approximated to the observed spectrum (besides that it provides a solution within the models base). The goodness of both fitting procedures can be quantified by the values derived for the χ^2_{red}. We also consider an additional quality indicator, the *adev*, that gives the percentage mean deviation over all fitted wavelengths (Cid Fernandes et al. 2013):

$$\text{adev} = \frac{1}{N} \sum_{i=1}^{N} \frac{|F_{obs,\lambda_i} - F_{mod,\lambda_i}|}{F_{obs,\lambda_i}}. \quad (4)$$

In Fig. 5, we present the distribution of the adev and the minimum χ^2_{red} values derived for all the samples (except for the galaxies Mrk 3, NGC 1097, NGC 1566, NGC 4594, NGC 5033 and NGC 7679 that present values χ^2_{red} and MAP > 50). For more than 50 per cent of the adjusted models, we found χ^2_{red} values less than 5, which can be classified as satisfactory adjustments. Also, the deviation between the observation and the best model fitted is less than adev $\lesssim$20 per cent for the majority of objects. In general, Figs 4 and 5 indicate that the χ^2_{red} method provides more satisfactory adjustments than the MAP using the BayesCLUMPY. This is the reason why we have chosen to only discuss the χ^2_{red} results in the next sections, however it is worth to note that the Bayesian technique has the advantage that one can use a-priori informations and it provide the posterior distributions of the parameters.

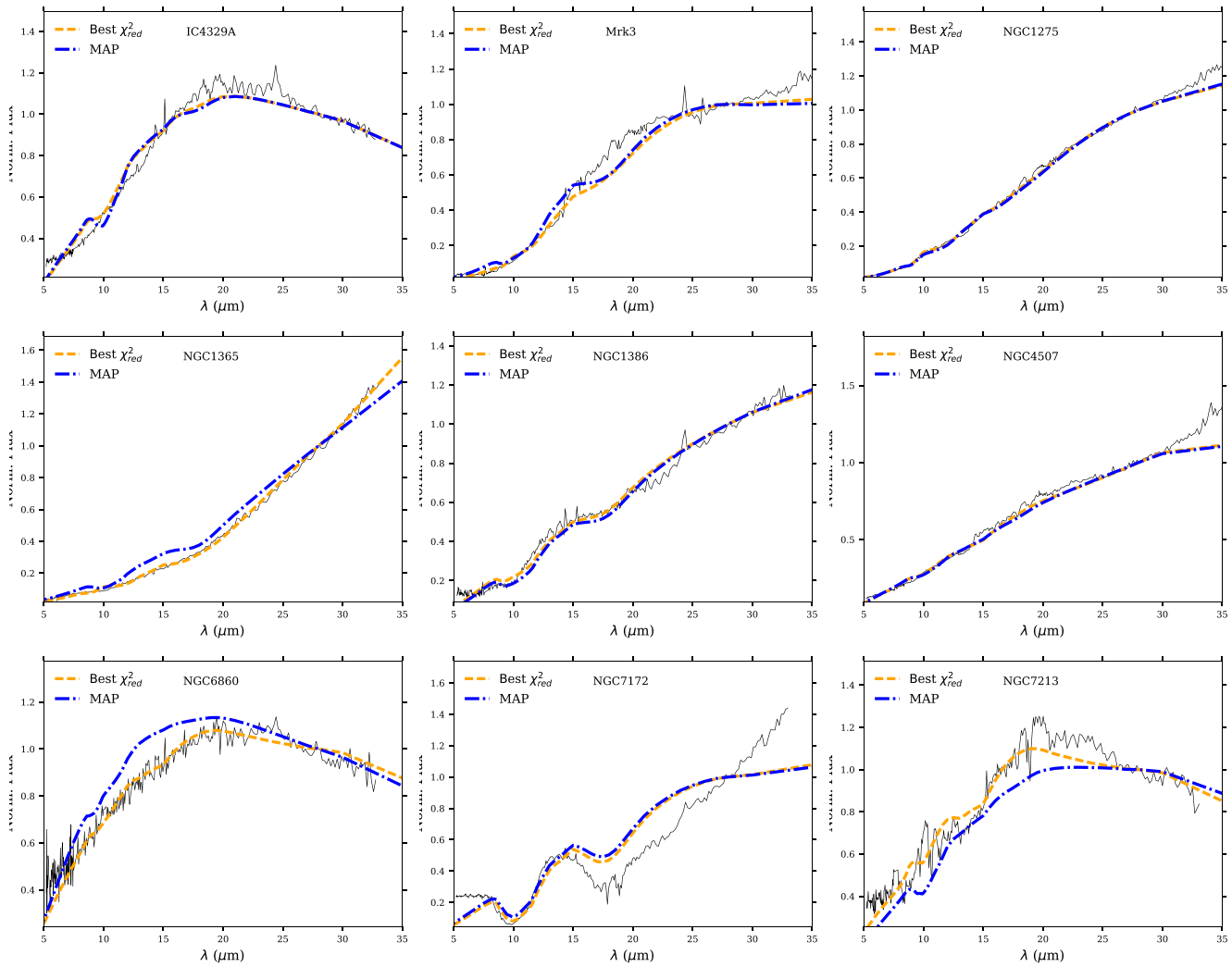

Figure 4. Examples of adjustments for the best fit using $\chi^2_{\rm red}$ and the maximum a posteriori distribution from BayesCLUMPY. Best torus fitting to the spectrum is represented by the yellow dashed line for the former and by the blue dot–dashed line in the latter case. The observed spectra and the SED models are normalized at 28 μm.

4 COMPARISON BETWEEN TYPE 1 AND TYPE 2 SOURCES

In order to compare the two fitting methodologies, we decided to consider the best solution of the $\chi^2_{\rm red}$ test and the MAP provided by the BayesCLUMPY method. However, it is important to notice that the model interpolations performed in BayesCLUMPY allow for a grid of parameters different from the ones provided by the CLUMPY torus models and listed in Table 1.

4.1 Direct parameters

Both fitting methodologies allow for the determination of parameters within the model set, what we call *direct parameters*. The values obtained for those parameters are presented in frequency histograms (Fig. 6), and the obtained mean parameters are listed in Table 2. We have chosen to discuss the results obtained with the $\chi^2_{\rm red}$ methodology; however, for completeness we will keep in all the histograms the results obtained with the BayesCLUMPY MAP mode. Below we discuss the results of each parameter individually.

It can be seen from Fig. 6 that the inclination angle relative to the observer's LOS, i, appears to be larger for Sy 2 ($\bar{i}$(Sy2) = 64.°5 ± 28.°3) than for Sy 1 ($\bar{i}$(Sy1) = 50.°6 ± 31.°4). This parameter was studied in previous works, with controversial results. RA11 studying a sample of 7 Sy 1 and 14 Sy 2 galaxies and from the 13 objects presented in AH11 sample found no significant differences in this parameter and suggested that type 2 objects could be seen in any orientation if there is at least one cloud obscuring the observer's LOS. On the other hand, Mor et al. (2009) studying 26 type 1 Palomar-Green (PG) quasars using *Spitzer* data found $\bar{i}$ = 33° while Lira et al. (2013) obtained a typical value of $i \gtrsim 40$ for a sample of 27 Sy 2 with about half of their sample requiring values $i \sim 70°$–$90°$. Our mean results for this parameter suggest that Sy 1s do present a slightly lower value for i than Sy 2s, supporting the viewing angle orientation requirement for the AGN's unified model. Likewise the CLUMPY models, the dusty clouds follow a Gaussian-like distribution along the equatorial ray characterized by a torus angular width (σ). Our results show that there are no significant differences for the mean σ values in the different types of activity, being $\bar{\sigma}$(Sy 1) = 36.°4 ± 19.°2 and $\bar{\sigma}$(Sy 2) = 43.°7 ± 20.°5. Taking only the mean values into account, these results may

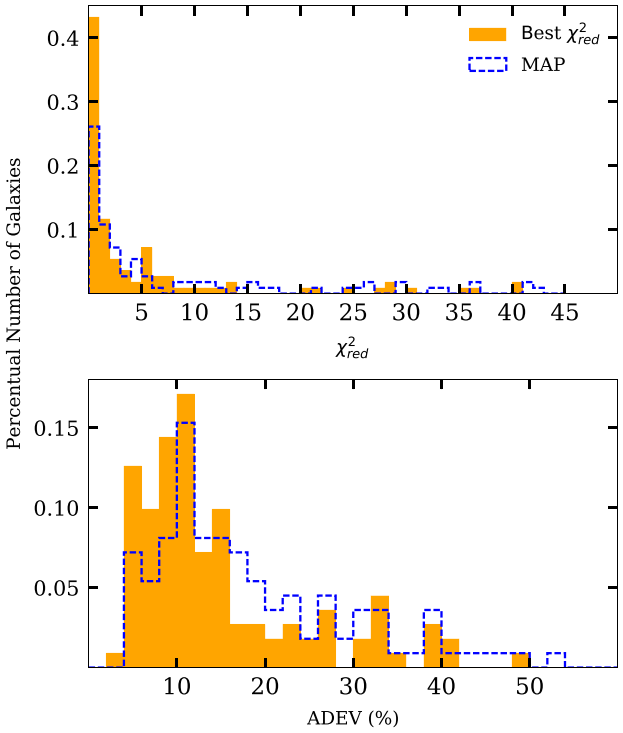

Figure 5. We show the values derived for the $\chi^2_{\rm red}$ (top panel) and the adev (bottom panel) that quantify the goodness of the $\chi^2_{\rm red}$ and the BayesCLUMPY fitting techniques. The orange filled histograms represent the values derived using the $\chi^2_{\rm red}$ technique while the blue dashed lines represent the distribution of the MAP values derived using the BayesCLUMPY method.

indicate that the torus hosted by Sy 1s is biased towards smaller values than those found in Sy 2s. In fact, these values agree with those found by RA11 and are further supported by the findings of Lira et al. (2013, $\sigma > 40$, for 70 per cent of their Sy 2) and Mor et al. (2009, $\bar{\sigma} = 34$, for their type 1 sources). Regarding the number of clouds along the LOS, we found that both types are well represented by $\sim$10 clouds [$\bar{N}$(Sy 1) $= 9 \pm 5$ and $\bar{N}$(Sy 2) $= 10 \pm 4$]. In the case of quasars, this number seems to be smaller ($\sim$5) than in the case of Seyfert galaxies (e.g. Mor et al. 2009; Lira et al. 2013). Thus, our findings reinforce the scenario proposed by AH11

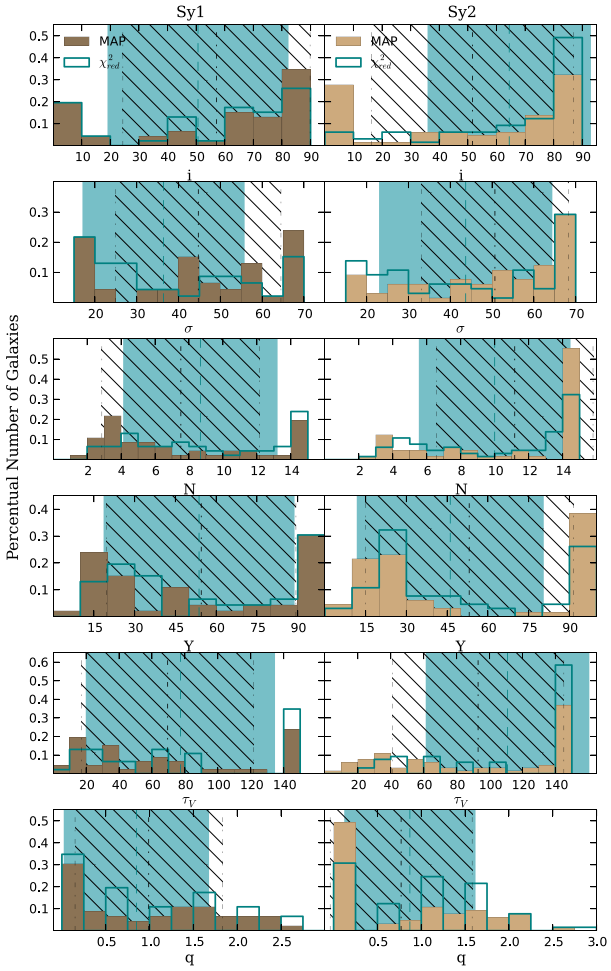

Figure 6. The frequency histogram distribution for direct parameters, i, σ, N, Y, $\tau_{\rm V}$ and q, derived from the CLUMPY model fitting. The brown filled histograms represent the MAP distributions resulting from the employing of the BayesCLUMPY task and the stepped blue distribution shows the results of the best solution applying the $\chi^2_{\rm red}$ test. In all panels, the distributions for the 46 Sy 1 are plotted at the left side and for the 65 Sy 2 at the right side. The dot–dashed lines indicate the mean value of the MAP distribution and the hatched areas delineate the mean values from the $\chi^2_{\rm red}$ and the uncertainties around the average.

Table 2. Mean parameters derived from the $\chi^2_{\rm red}$ and MAP of CLUMPY model fitting .

Parameter	$\chi^2_{\rm red}$		MAP	
	Sy 1	Sy 2	Sy 1	Sy 2
		Direct		
i	50.6 ± 31.4	64.5 ± 28.3	57.1 ± 32.7	51.6 ± 35.3
σ	36.4 ± 19.2	43.7 ± 20.5	44.7 ± 19.8	50.7 ± 17.6
N	9.0 ± 5.0	10.0 ± 4.0	8.0 ± 5.0	11.0 ± 5.0
Y	53.7 ± 34.9	46.1 ± 34.1	54.5 ± 34.9	53.1 ± 38.3
$\tau_{\rm V}$	77.3 ± 57.0	110.9 ± 49.2	69.5 ± 52.2	93.0 ± 52.1
q	0.8 ± 0.8	0.9 ± 0.7	1.0 ± 0.8	0.8 ± 0.8
		Indirect		
$N_{\rm los}$	3.0 ± 4.0	7.0 ± 5.0	4.0 ± 4.0	6.0 ± 5.0
$A_{\rm V}$	287 ± 595	899 ± 829	241 ± 509	671 ± 799
$\log(N_{\rm H}/{\rm cm}^{-2})$	23.7 ± 24.1	24.2 ± 24.2	23.7 ± 24.0	24.1 ± 24.2
$P_{\rm esc}$	0.3 ± 0.3	0.1 ± 0.2	0.2 ± 0.3	0.1 ± 0.2
$C_{\rm T}$	0.7 ± 0.2	0.8 ± 0.2	0.8 ± 0.2	0.9 ± 0.2
$M_{\rm tor}$~($M_\odot$)	$2.1 \pm 3.9 \times 10^6$	$2.7 \pm 5.5 \times 10^6$	$2.4 \pm 3.7 \times 10^6$	$3.5 \pm 6.0 \times 10^6$

in which the number of clouds might be in an evolutionary stage of a receding torus.

Besides the above parameters, other fundamental parameter is the torus thickness, Y, which is calculated as the ratio of the outer R_o to inner radius R_d, $Y = R_o/R_d$, where R_d is set as being the distance from the central source where dust sublimates and according to Barvainis (1987) can be obtained by

$$R_d = 0.4\left(\frac{L_{AGN}}{10^{45}\ \mathrm{erg^{-1}}}\right)^{0.5}\left(\frac{1500\,\mathrm{K}}{T_{sub}}\right)^{2.6}\ \mathrm{pc} \quad (5)$$

with T_{sub} being the dust sublimation temperature and L_{AGN} is the AGN bolometric luminosity. The values we derived for the torus thickness do not present any significant distinction on average values and also for the shape of the distribution, as can be seen in Fig. 6. For both classes, we can find solutions at the edges of the distribution, indicating that the majority of objects require a very large value of Y or a compact torus. In this case, the mean values derived ($\bar{Y}(\mathrm{Sy\,1}) = 53.7 \pm 34.9$ and $\bar{Y}(\mathrm{Sy\,2}) = 46.1 \pm 34.1$) do not represent the sample.

In fact, as pointed out by Nenkova et al. (2008b), when $q = 2$ the IR fitting leads to a poor constraint on the torus extension since the clouds are distributed close to R_d. Therefore, RA11 and AH11 have chosen to restrict this parameter according to observations that suggest smaller values for the torus radial extension ($Y \sim$ 10–20; Jaffe et al. 2004; Tristram et al. 2007; Raban et al. 2009). We also performed our MIR fitting using the same constraint of Y[5,30] adopted in AH11 and still our findings do not imply significant changes on the other parameters' distribution. Hence, we decided to maintain the original Y parameter space since this bimodality found in our results can be attributed to a better constraint on $\gtrsim$20 μm Fuller et al. (2016) show that the inclusion of SOFIA photometric data in the 30–40 μm wavelength range helps to better constrain Y. This is because the outer radius R_o is more sensitive to the cooler dust that peaks in the far-IR, providing information about the torus size.

Due to computational limitations, the CLUMPY models assume that all dust clouds have the same optical depth, τ_V (see Nenkova et al. 2008b, for details). It is clear from Fig. 6 that the distribution of individual cloud's optical depth points is centred on high values of τ_V. Also, approximately 60 per cent of the solutions for Sy 2 galaxies require $\tau_V \sim 140$ mag, presenting an average value of $\bar{\tau_V}(\mathrm{Sy\,2}) = 111 \pm 49$ mag for type 2 sources, while for Sy 1 we found a smaller value of $\bar{\tau_V}(\mathrm{Sy\,1}) = 77 \pm 57$ mag. Both results are in agreement with the high optical depth condition ($\tau_V \gtrsim 60$) of the CLUMPY models, which requires such values to ensure that we do have optically thick clouds and a finite photon escape probability. However, for this parameter, our results differ from those found in the literature, which derive lower values of τ_V for Sy 2 galaxies; for example, for the 14 Sy 2 sample of RA11 the typical values derived are $\tau_V \sim 30$ mag, and for the 27 Sy 2 from Lira et al. (2013) the best solutions in general assume lower values ($\tau_V \lesssim 25$ mag). We also tested for a possible correlation with τ_V and the galaxy inclination and no correlation was found.

In the CLUMPY model, the cloud distribution is described by a power law of form r^{-q}. The histograms with the index (q) distribution for both types of activity show that the solutions are found to be more likely within lower values for this parameter, generally between $0 < q < 1$. Values of $q \sim 0$ indicate a constant distribution, revealing that the number of clouds presents a weak dependence on the distance to the central AGN, while values $q \sim 1$ point to a distribution following a $1/r$ relation. The average values derived for both classes are quite similar for both types of activities, being $\bar{q}(\mathrm{Sy\,1}) = 0.8$ and $\bar{q}(\mathrm{Sy\,2}) = 0.9$. Our results follow the same trend as found by Mor et al. (2009, $\bar{q} = 1$) and also by Lira et al. (2013, $q \sim 0$) since the distribution for this parameter is quite spread as can be seen in the histograms in Fig. 6, where more than 30 per cent of the sample present values of $q = 0$.

Table 3. The K–S test for the parameter distribution of Sy 1 and Sy 2.

Parameter distribution	D	p-value
i	0.44	0.25
σ	0.18	0.99
N	0.33	0.31
Y	0.20	0.97
τ_V	0.27	0.59
q	0.17	0.99

We also performed a two-sample Kolmogorov–Smirnov (K–S) test (von Mises 1964) in order to verify the results discussed above and quantify the differences between the parameter distribution for both activity types. The K–S test determines if the Sy 1 and Sy 2 parameters have the same distribution and the values derived for D, i.e. the supremum of the cumulative distribution functions (CDFs) of the Sy 1 and Sy 2 for each CLUMPY parameter, and p-value are shown in Table 3. As we can see, the inclination i presents a significant discrepancy between the CDFs since the D value is the most considerable among the other CLUMPY parameters, followed by N and τ_V. Since in both activity types we found $N \sim 10$, the main parameters to classify an Sy 1 or an Sy 2 rely on a combination of i and τ_V: it depends on the observers' LOS orientation as well on the obscuring properties of the clouds. On the other hand, the p-values for σ, Y and q suggest that Sy 1 and Sy 2 populations are drawn from the same distribution, e.g. we cannot distinguish whether a distribution of the geometrical parameters σ, Y and q is from an Sy 1 or an Sy 2.

Some objects in our sample are common to previous works of RA09 (9 objects), AH11 (14 objects), RA11 and Lira et al. (2013, 20 objects). In general, our mean results are in good agreement with the literature, although the individual solutions may be quite different. We attribute these differences to the fact that each study used distinct approaches (for example, wavelength coverage, resolution, parameter constrains, methodology). For instance, that may also explain the differences in the reported parameters for the same galaxy in different papers by the same authors. In addition, our results in general tend to be more consistent with those presented by Lira et al. (2013). As pointed out by the latter, there are very significant differences in the results found between RA11 and AH11 attributed to the inclusion of the 10 μm spectroscopic observations. Since the silicate at 9.7 μm is an important dust feature, the inclusion of detailed spectral information around this feature is crucial to properly describe the physical parameters from the SEDs.

In order to illustrate a mean SED and torus physical representation, we present a sketch in Fig. 7 that shows the mean theoretical SEDs from CLUMPY to create a representative SED for each type of activity. There we combine the mean parameters derived in Table 2. We also illustrate a schematic cross-section view of the tori for both activity types, in order to highlight the differences in the torus physical properties, for instance, the slightly larger radial thickness for Sy 1 and the wider angular width in Sy 2, consequently (given the Gaussian distribution) increasing the number of clouds in this type. These results are in agreement with the results of RA11 who found that the tori of Sy 1s are narrower and with fewer clouds than

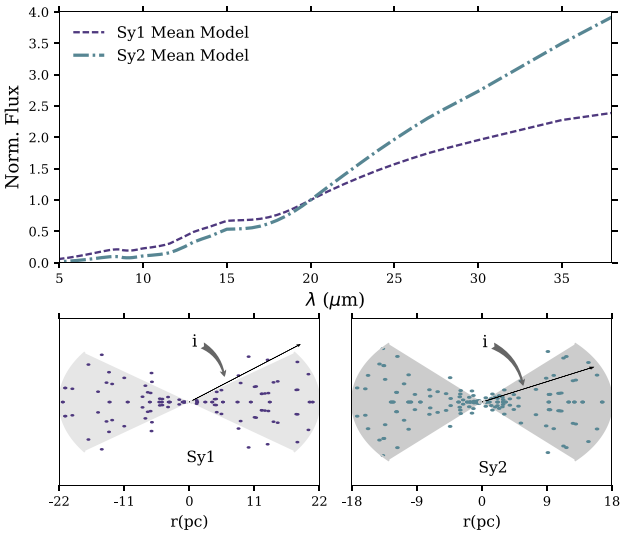

Figure 7. Combination of the mean parameters from CLUMPY theoretical SEDs, represented by the dashed purple line for Sy 1 and the dot–dashed blue lines for Sy 1. A schematic torus cross-section is also illustrated in order to feature the main differences between the torus physical properties.

those found in Sy 2s. Furthermore, the mean SEDs do not present a turnover of the torus emission, predicted to occur between 30 and 50 μm. This result is in agreement with those found by Fuller et al. (2016), where no turnover was observed below 31.5 μm. Further nuclear far-IR observations would be essential to determine the peak of the IR emission, giving insight into the torus outskirts.

4.2 Indirect parameters

As mentioned before, the model geometry enables us to estimate other important parameters that may help us to understand the physical properties of the putative torus required by the unified model. The distribution derived for the indirect parameters is described below and presented in Fig. 8 as well as the information about mean values is summed up in Table 2 and described in the text. It is worth mentioning that all these indirect parameters were obtained using the results of the best direct parameters described in the previous section.

Since we are dealing with a clumpy medium, one of the most important parameters in describing the torus is the number of clouds blocking our LOS ($N_{\rm los}$). By using the model cloud distribution (with a Gaussian like form), centred at the equatorial plane, we can compute the number of clouds along any specific direction; thus, if we choose the LOS direction, we can compute $N_{\rm los}$ (equation 1). The $N_{\rm los}$ distribution is shown in the top panel of Fig. 8; by inspecting this figure, it is clear that the number of clouds along the observer's LOS presents a sharp peak in its distribution for Sy 1 (centred at ∼3), while a spread distribution is found for Sy 2 ($\bar{N_{\rm los}} = 7$). At the same level of importance is the extinction of the light caused by the material composing the LOS clouds. Once $N_{\rm los}$ is known, the total optical depth along the LOS is obtained with equation (2). The distribution of $A_{\rm V}$ is well defined for Sy 1, with small values, while in Sy 2 it is flat. In addition, the determination of $N_{\rm los}$ is also related with the X-ray columnar hydrogen density that can be derived using the standard Galactic ratio and the foreground extinction from Bohlin, Savage & Drake (1978) via $N_{\rm H}/A_{\rm V} = 1.9 \times 10^{21}$ cm^{-2}. In agreement with the two previous indirect parameters, the $N_{\rm H}$ is

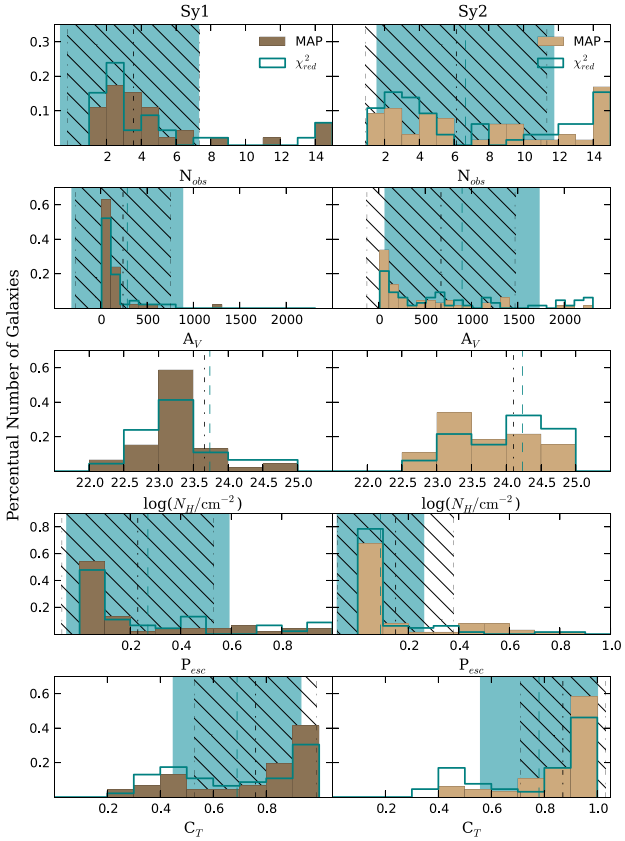

Figure 8. The frequency histogram distribution for indirect parameters, $N_{\rm los}$, $A_{\rm V}$, $N_{\rm H}$, $P_{\rm esc}$ and $C_{\rm T}$, derived from the CLUMPY model fitting. The brown filled histograms represent the MAP distributions resulting from the employing of the BayesCLUMPY tool and the stepped blue distribution shows the results of the best solution applying the $\chi^2_{\rm red}$ method. The panels follow the same scheme as listed in Fig. 6.

well defined for the Sy 1 galaxies ($\bar{N_{\rm H}} = 5 \times 10^{23}$ cm^{-2}) and with a not-so-centred distribution for Sy 2s ($\bar{N_{\rm H}} = 1.6 \times 10^{24}$ cm^{-2}).

These results together with the fact that we are not finding significant difference in the observer's viewing angle for the different classes point to the fact that the most important parameter in determining if a galaxy is classified as a type 1 or 2 object is if there are clouds able to block the radiation from the BLR and central engine. This suggests that the fundamental requirements of the unified model for AGNs depend more on the intrinsic parameters of the torus than on its geometry. In fact, our results support the finding of RA11 who found significant differences in the torus angular size for the different classes. However, in contradiction with our results, they do find lower optical depth in Sy 2 when compared with Sy 1.

One of the fundamental requirements of the unification schemes is that a photon generated in the accretion disc is able to escape through the torus. Thus, a fundamental parameter that can be derived from Nenkova et al. (2008b) formalism is the escape probability, $P_{\rm esc}$. This parameter can work as an estimator whether an object is type 1 or type 2 since the putative large viewing angles in the latter are associated with the probability to have more clouds blocking the AGN radiation, leading to a finite but small probability of direct view to the AGN. When the condition $\tau_{\rm V} \gg 1$ is achieved, $P_{\rm esc}$ can be estimated as

$$P_{\rm esc} \cong {\rm e}^{-N_{\rm los}}. \quad (6)$$

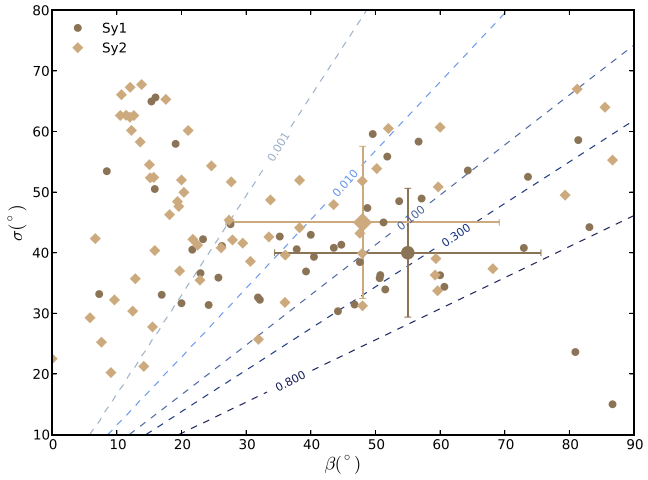

Figure 9. Illustration of the distribution of P_{esc}, the photon escape probability, as a function of the torus width, σ, and the complementary viewing angle, $\beta = \pi/2 - i$, related to equation (6). In agreement with the unified model premise, which expect that Sy 2 galaxies are more likely on the left side and Sy 1 on the centre of the graph and higher P_{esc} values, we found that Sy 2s are more concentrated at lower probabilities, except for some objects. As a representative value for our sample, we utilized $N = 10$ to plot the P_{esc} curves.

The frequency histograms showing the P_{esc} are presented in Fig. 8. The results agree with the predictions (i.e. lower probabilities are expected in type 2 objects). We found mean values of $\bar{P}_{esc}(\mathrm{Sy\,2}) = 0.1$ and $\bar{P}_{esc}(\mathrm{Sy\,1}) = 0.3$ indicating that, on average, a photon originated in the central source has an ∼30 per cent chance to escape from the torus without being absorbed. The individual cloud emission, as adopted in the CLUMPY model formalism, plays a fundamental role in understanding the emerging IR torus radiation. It can be originated by clouds directly illuminated by the AGN photons and the reprocessed radiation from the shaded side of clouds which are heated by the emission of more internal clouds. Thus, what is observed is a sum of the radiation emitted by the torus and the photons generated in the accretion disc that are able to scape (i.e. P_{esc}); therefore, knowing P_{esc} is fundamental to determine the whole SED emission.

Once P_{esc} is a non-linear function of σ, β and N, we used the results we obtained with our *Spitzer* data fittings for σ and β and adopted a value for $N = 10$ in order to determine P_{esc} curves in the $\sigma \times \beta$ plane following the analysis performed by AH11. The results are shown in Fig. 9; for display purposes for this figure, we used a 10 per cent of χ^2_{red} deviations as described in Sales et al. (2013). It emerges from this figure that most of the Sy 2 galaxies present $P_{esc} \lesssim 10$ per cent. The distribution of P_{esc} is quite broad for Sy 1, which may be a reflection of the fact that both σ and β do present a variety of values in this class (see Fig. 6). This parameter was also studied by RA11 and AH11; our results are in good agreement with those found by these authors, in the sense that there is a significant difference between both types of activities. However, while we find almost the same fraction for Sy 1s, we find larger values for Sy 2s than the values found by these authors. We attribute this difference (in type 2 objects, $P^{we}_{esc} = 10$ per cent and $P^{they}_{esc} = 0.1$ per cent) to the fact that they restricted the torus thickness ($5 \leq Y \leq 30$) and we allow it to take all the possible values.

Another parameter provided by the model is the geometrical covering factor that can be understood as the sky fraction at the AGN centre which is being obscured by the dusty clouds. This parameter can be determined by integrating the P_{esc} over all orientations, following the equation (Nenkova et al. 2008a)

$$C_T = 1 - \int_0^{\pi/2} P_{esc}(\beta)\cos(\beta)\mathrm{d}\beta. \quad (7)$$

The distribution of the derived values for C_T is presented in Fig. 8. We found slightly larger C_T values for type 2 sources ($\bar{C}_T(\mathrm{Sy\,2}) = 0.8 \pm 0.2$) than for type 1 galaxies ($\bar{C}_T(\mathrm{Sy\,1}) = 0.7 \pm 0.2$). Our values are in agreement with the literature in the sense that there is a difference between both activities; however, while RA11 find typical values of 0.5 for the Sy 1 in their sample, these authors find almost the same values we found for the Sy 2 in their sample. Mor et al. (2009) also found an even smaller (∼0.3) mean value in their type 1 PG quasars sample.

According to Nenkova et al. (2008a), the definition of C_T arises from the geometry and probabilistic nature of a clumpy medium and can be interpreted as the fraction of randomly distributed observers whose view to the central source is blocked or as the fraction of type 2 objects in a random sample. The covering factor can also be decisive in AGN classification because an AGN with a larger covering factor has a higher probability to be viewed as type 2. Many questions are still opened concerning the definition of the intrinsic covering factor if the geometrical one is related with the 'dust' covering factor proposed by Maiolino et al. (2007, defined as the ratio between the thermal component and the AGN contributions). Since the covering factor measures the fraction of AGN luminosity captured by the torus and converted to IR, the AGN IR luminosity is $C_T L_{bol}$, where L_{bol} is its bolometric luminosity (Elitzur 2012). Thus, it is expected that type 2 AGNs have intrinsically higher IR luminosities than type 1. However, in disagreement with earlier expectations of a strong anisotropy at $\lambda \lesssim 8$ μm, *Spitzer* observations present very similar IR fluxes of types 1 and 2 as shown by Lutz et al. (2004) and Buchanan et al. (2006), which can be partly explained by a clumpy torus distribution.

The geometrical C_T can be interpreted as the 'true' torus covering factor because it is independent of i. However, on the other hand, as can be noted from equation (7), C_T depends on N and σ; thus, to investigate this relation, we show in Fig. 10 the results of the models fits[6] in the N–σ plane together with the contour plots of C_T (accordingly to Fig. 10 from RA11). We found that type 2 objects do preferentially lie on the top right of the figure, or in other words they do have large C_T values. However, in the case of type 1 objects (where low C_T values are expected since the BLR emission should be observable), we found that they are spread over the whole plane. AH11 and RA11 suggest that type 1 and type 2 AGNs preferentially are located in different regions on the plane (with type 1 having lower values than type 2); however, we do not see this trend in our work because, despite the same results for the σ, we derived larger values for the number of clouds, N, and therefore it is expected that more clouds obscure the central source. Since C_T is very sensitive to N and σ, our results always point to higher values than those found in their sample. We would also like to emphasize that our sample consists of a larger, thus more statistically representing sample. This trend may be biased since we do use data with lower angular resolution (thus more uncertain) and the other works have a smaller sample, but with high angular resolution, or due to the restrictions in the parameter space adopted by the authors.

[6] For display purposes, we adopted the mean values of each parameter for the 10 per cent deviation of the best χ^2_{red}.

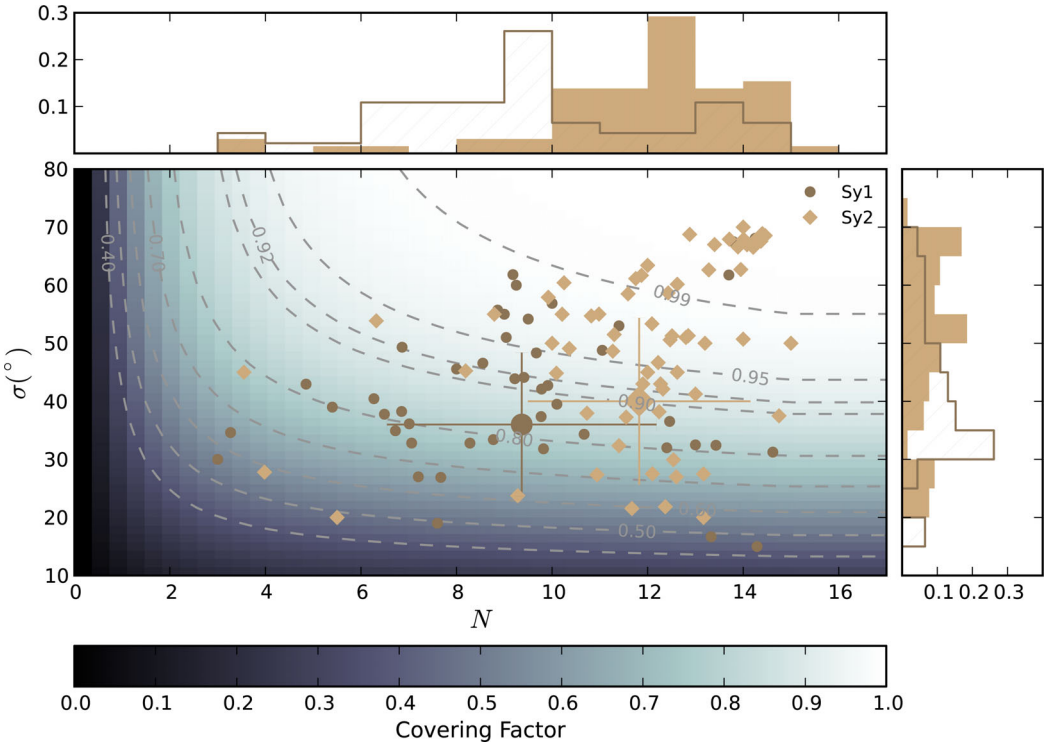

Figure 10. Illustration of the distribution of N and σ and their correlation with the covering factor, C_T. Covering factor curves are shown for values from 0.2 to 0.9 according to equation (7). The closed diamonds represent the Sy 1 objects and the circles show the Sy 2 types. The histograms for N and σ are attached at the top and right side of the main plot, respectively, for both activity types. As argued in Elitzur (2012), the Sy 2 galaxies are more likely drawn from the distribution of higher covering factors than Sy 1 types (e.g. see also Fig. 10 from RA11).

4.3 Torus mass and size

Beside the above torus parameters, the CLUMPY formalism also allows us to determine the mass of the emitting hot dust, as well as to set some constrains on the torus size. From the adjustment of the theoretical SED CLUMPY model, the bolometric luminosity of the AGN, L_{AGN}, can be found from the scalefactor (Θ) of the model to the observation, by solving the equation

$$\lambda_{obs} F_{obs,\lambda} = \Theta \frac{\lambda_{mod} F_{mod,\lambda}}{F_{AGN}}. \quad (8)$$

We can derive L_{AGN} applying the distance relation $L_{AGN} = 4\pi D^2 \Theta$ and once it is calculated equation (5) can be used to estimate the inner radius assuming a sublimation temperature for the silicate grains (we used $T_{sub} = 1500$ K). The torus dimension is estimated by the relation $Y = R_o/R_d$, where Y is taken from the best fit. In order to test the L_{AGN} values derived from the scaling of the CLUMPY models, we can compare them with those reported in the literature for the X-rays by applying the bolometric correction of ∼20 (Elvis et al. 1994), and the comparison between the fitted and literature L_{AGN} is shown in Fig. 11. As can be seen from the one-to-one line, the observed and calculated values do agree well.

Fig. 12 shows histograms for the distributions of L_{AGN} and R_o. No significant differences between type 1 and type 2 galaxies are seen. In general, the estimated values of the AGN bolometric luminosity range between $42 < \log(L_{AGN}) < 46$, and the average values in both classes are typically $L_{AGN} \sim 10^{44}$. For the sublimation radius, we find averages $R_d(\mathrm{Sy\,1}) = 0.12$ pc for Sy 1 galaxies and $R_d(\mathrm{Sy\,2}) = 0.16$ pc for Sy 2, which lead to average torus sizes very close to those found in the literature (RA09; AH11; RA11; Lira et al. 2013), with typical values of $R_o \lesssim 6$ pc. These results are further supported by observational evidences. For instance, previous works using MIR interferometric observations provide information on a relatively compact torus, with a few parsec scale (Jaffe et al. 2004; Tristram et al. 2007, 2009; Burtscher et al. 2009).

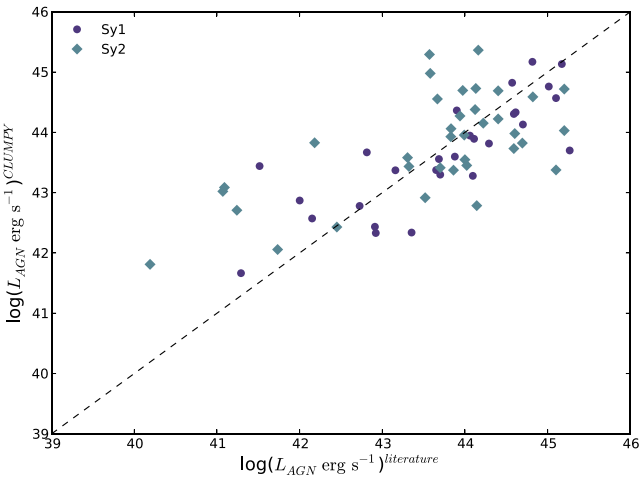

Figure 11. Comparison between the bolometric luminosities, L_{AGN}, derived from the CLUMPY models with those reported in the literature for the hard X-ray luminosities, L_X, applying the bolometric corrections of Elvis et al. (1994). The diamonds represent the Sy 1 objects while the circles indicate the Sy 2 types and the dashed line indicates the identity line.

By adopting some approximations for the torus geometry and size, we can also estimate its total mass. Considering the mass of a single cloud as $m_H N_{H,c} A_c$, where $N_{H,c}$ is its column density and A_c its cross-sectional area, the total mass in clouds is given by

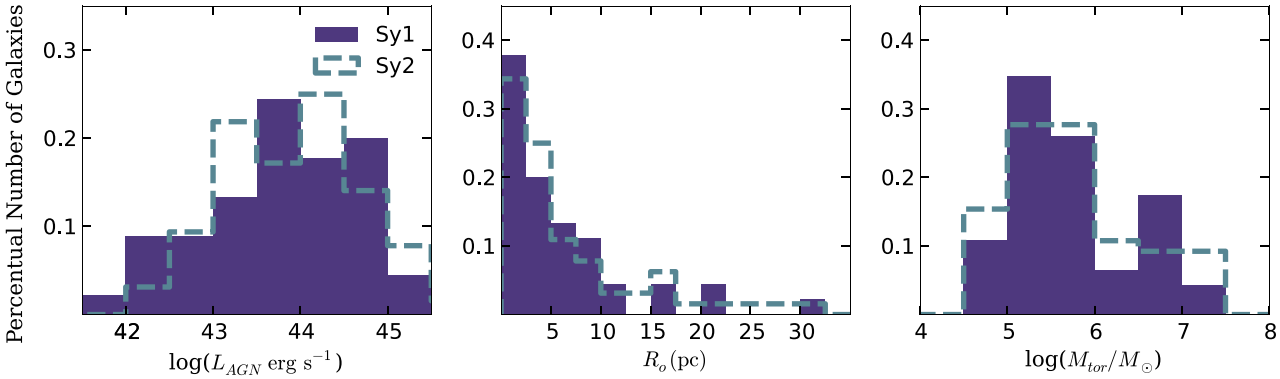

Figure 12. The histograms show the distribution of the AGN bolometric luminosities (left-hand panel), torus sizes R_o (the middle panel) and the torus masses M_{tor} (right-hand panel). Histograms filled in purple represent the distributions for Sy 1 and dashed lines in blue indicate the distributions for Sy 2.

$M_{tor} = m_H N_H{}^1 \int \eta_c(r, \beta) dV$, where $\eta_c(r, \beta)$ indicates the cloud distribution profile. For simplicity, assuming a sharp-edge angular distribution, M_{tor} can be analytically calculated (Nenkova et al. 2008b):

$$M_{tor} = 4\pi m_H \sin(\sigma) N_H{}^{(eq)} R_d^2 Y I_q(Y), \quad (9)$$

where Y_q =1, $Y/(2\ln Y)$ and $Y/3$ for q = 2,1 and 0, respectively, and $N_H{}^{(eq)}$ is the mean overall column density in the equatorial plane. The latter can be estimated by multiplying the number of clouds along the equatorial ray N by a single cloud columnar density $N_{H,c} \sim 10^{22}$–10^{23} cm^{-2}. Finally, since $N \sim$ 5–15, $N_H{}^{(eq)}$ assumes typical values of $\sim 10^{23}$–10^{24} cm^{-2}.

We found that M_{tor} ranges from 10^4 to 10^7 M$_\odot$ in both activities with mean values typically with 10^6 M$_\odot$ (Fig. 12), in agreement with the estimation by Lira et al. (2013) and Mor et al. (2009) using the CLUMPY model formalism to derive M_{tor}. A recent work from García-Burillo et al. (2014) was able to constrain M_{tor} derived from CLUMPY model fitting with the mass of molecular outflow observations in NGC 1068 using ALMA observations in bands 7 and 9. They estimate $M_{tor} \sim 2 \times 10^5$ M$_\odot$, consistent with the estimated molecular gas mass detected inside the central aperture (r = 20 pc) derived from the CO(3–2) emission.

5 THE EFFECTS OF HOT DUST EMISSION

It is widely known that the inner torus radius is related with the dust grain sublimation temperature ($T \sim$ 800–1500 K). Such temperature peaks at NIR wavelengths and in the case of AGNs this emission is related with the dusty torus (Barvainis 1987; Rodríguez-Ardila & Mazzaly 2006; Riffel et al. 2009). Therefore, the inclusion of the NIR spectral region is crucial to probe the hotter and innermost regions of the torus.

In fact, Ramos Almeida et al. (2014) demonstrated the need of the inclusion of the NIR data to constrain the torus parameters, especially to constrain the torus radial extension, Y. In their work, they analysed a compilation from the literature of NIR+MIR photometry and MIR spectroscopy (8–13 μm) of six Seyfert galaxies. All the objects in their study share the same characteristics: undisturbed, face-on galaxies with no prominent emission of dust lanes. In particular, they recommend a minimum combination of data in the J+K+M-band photometry and the N-band spectroscopy.

In order to study the effects of the hotter and inner region of the torus, we included in our analysis *ZJHK*-band long-slit spectroscopy data for the 32 objects where such information was available in the literature. Data for 24 galaxies were obtained from Riffel, Rodríguez-Ardila & Pastoriza (2006). These data were collected using the SpeX spectrograph of the NASA 3 m Infrared Telescope Facility in the short cross-dispersed mode (SXD, 0.8–2.4 μm) using a slit of 0.8 arcsec × 15 arcsec slit. The used spectra are those of the nuclear extraction (sampling few hundred pc). For more details about the data, see Riffel et al. (2006, 2009). The remaining eight sources were taken from Mason et al. (2015); these spectra were observed using the Gemini Near Infrared Spectrograph (GNIRS) in the XD mode. This instrument also covers simultaneously the 0.8–2.4 μm wavelength range. The observations were performed using a 0.3 arcsec × 1.8 arcsec slit, and the spectral extractions correspond to regions of ∼150–370 pc in the galaxies. The objects with SpeX or GNIRS spectra available are reported in Table A1 of Appendix A.

The same methodology described in the previous sections was used to perform the fitting of the observed spectra to the theoretical CLUMPY models. Since both SpeX and GNIRS spectra have higher spectral resolution than the IRS/*Spitzer*, we rebinned the NIR spectra in 0.16 μm intervals in order to have the same sampling as the MIR. The χ^2_{red} minimization was applied once more to all 32 combination of NIR+MIR spectroscopic data. In Fig. 13, we present the individual results for each parameter considering all the solutions within 10 per cent deviation of the minimum χ^2_{red} and compare them with the results obtained when using only the *Spitzer* data.

It is shown that in most of the cases the distribution of Y is well constrained, even when only using the MIR data, despite some differences for the solution in individual galaxies. The preference for higher values of τ_V can be found in most of the galaxies. We can also notice that the inclusion of NIR data in general better constrains the torus width σ. In general, the distribution of the torus parameters using the NIR+MIR combination does not change dramatically compared with those found only using the IRS spectra.

Following the previous methodology, in order to study the main differences between type 1 and type 2 objects, we compared the mean results for the 19 Sy 1 and 13 Sy 2, as shown in Fig. 14 , obtained by including the NIR spectral range with that obtained if we only consider the MIR data. The only noticeable change is found for the clouds' radial profile for Sy 2s, where slightly higher values ($q \sim$ 1.5) are found when including the NIR spectral range in the analysis.

The inclusion of the NIR in our analysis does reinforce our previous results that the inclination angle to the observer is not the only relevant parameter to distinguish between the galaxy types. Instead, the combination of the observer's angle, the number of clouds and

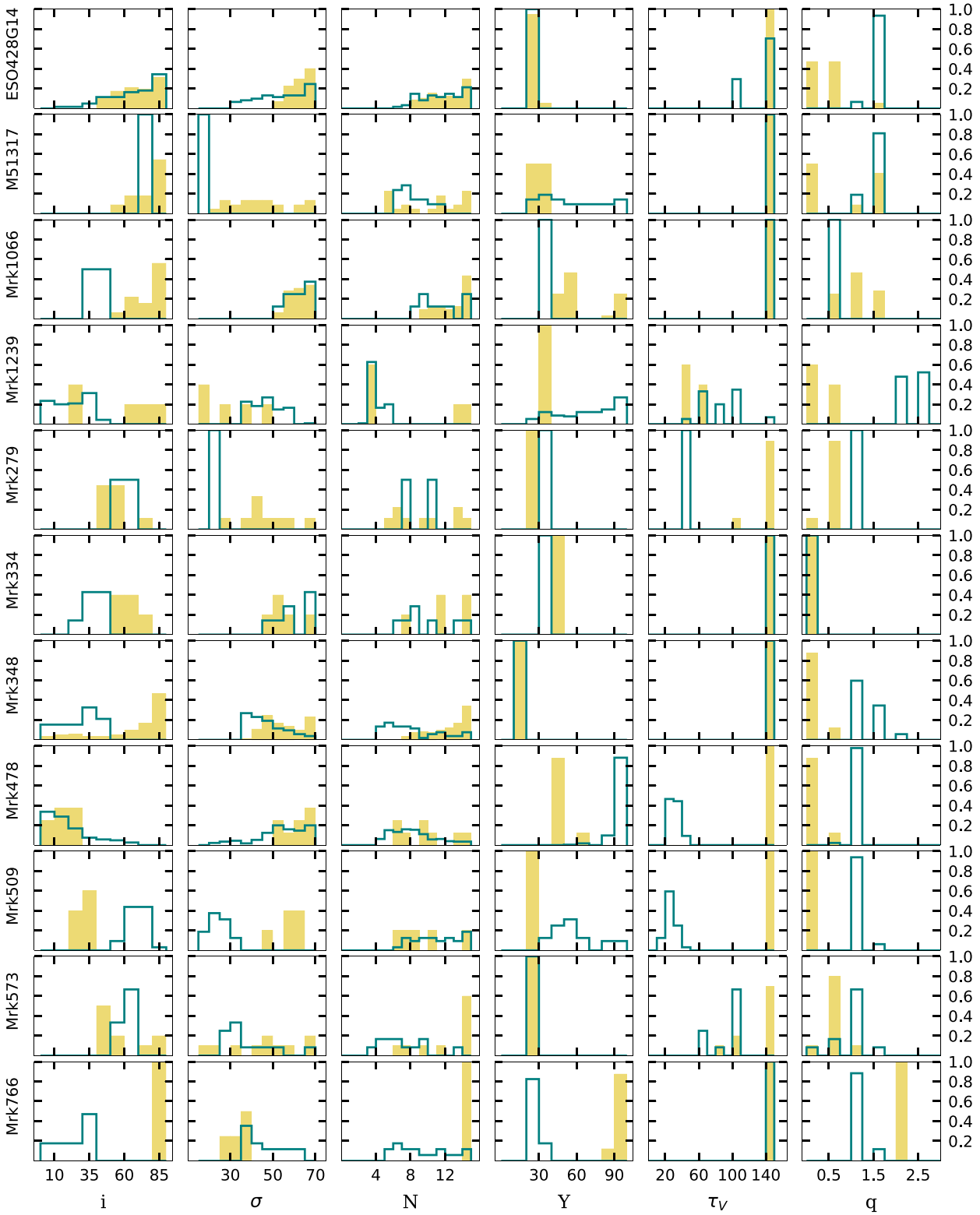

Figure 13. The individual distribution of the six CLUMPY parameters. The stepped histograms in blue show the parameter distribution of the *JHK* spectroscopic data and the IRS spectra, while the yellow filled histograms show the results only considering the MIR data.

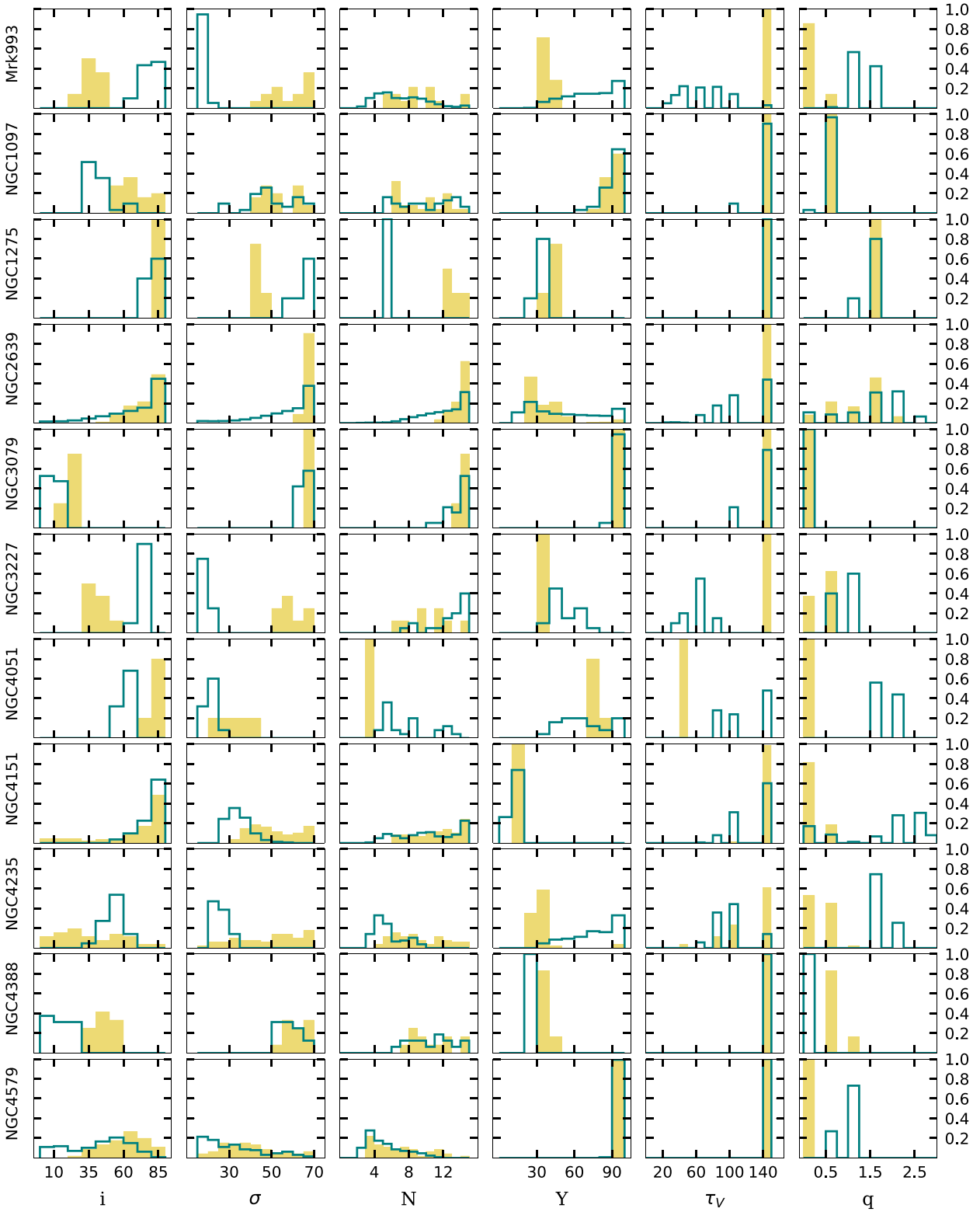

Figure 13 – *continued*

the physical properties of the clouds, described by the τ_V, plays a very important role in the classification. When analysed individually, in general the parameters are well constrained. However, when gathered and compared by type 1 and type 2, we found broad distributions, indicating a large dispersion of the parameter values in each type of activity. The main concern with our findings is the intrinsic degeneracy of the CLUMPY models since a combination of different parameters can reproduce almost the same SED.

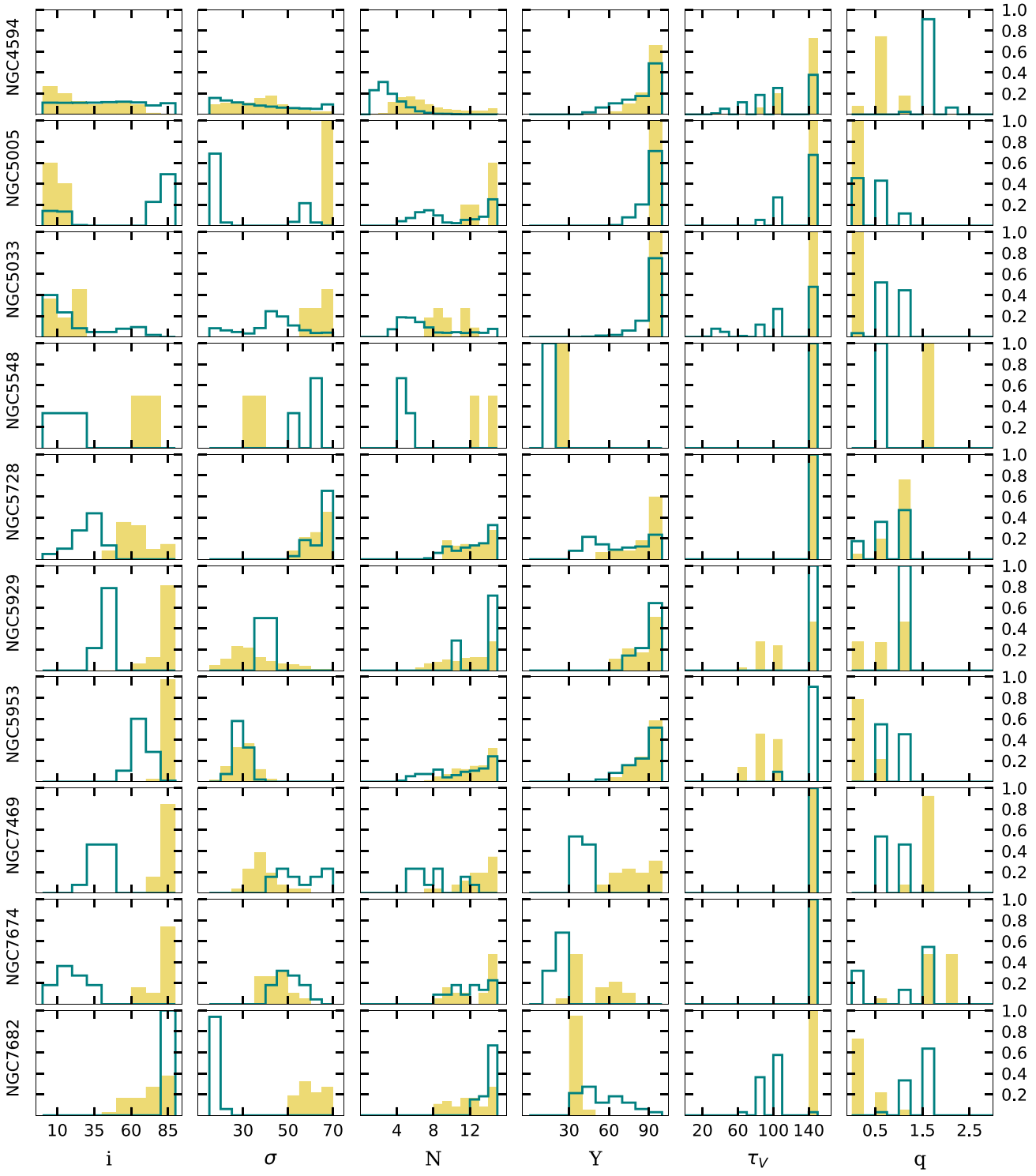

Figure 13 – *continued*

It is important to remark that the findings of Ramos Almeida et al. (2014) are very relevant in order to constrain all the torus parameters, but they represent a small and very particular sample, without prominent dust emission and face-on galaxies. Our work aimed at exploring the generality of the CLUMPY models since they are reproducing only the torus emission and in principle they should represent any galaxy scenario. These results reinforce the fact that we are dealing with the probabilistic nature of a clumpy environment.

We would like to highlight the importance of the use of a large and homogeneous sample in order to determine in a reliable way the torus properties. One of the main problems when analysing SEDs

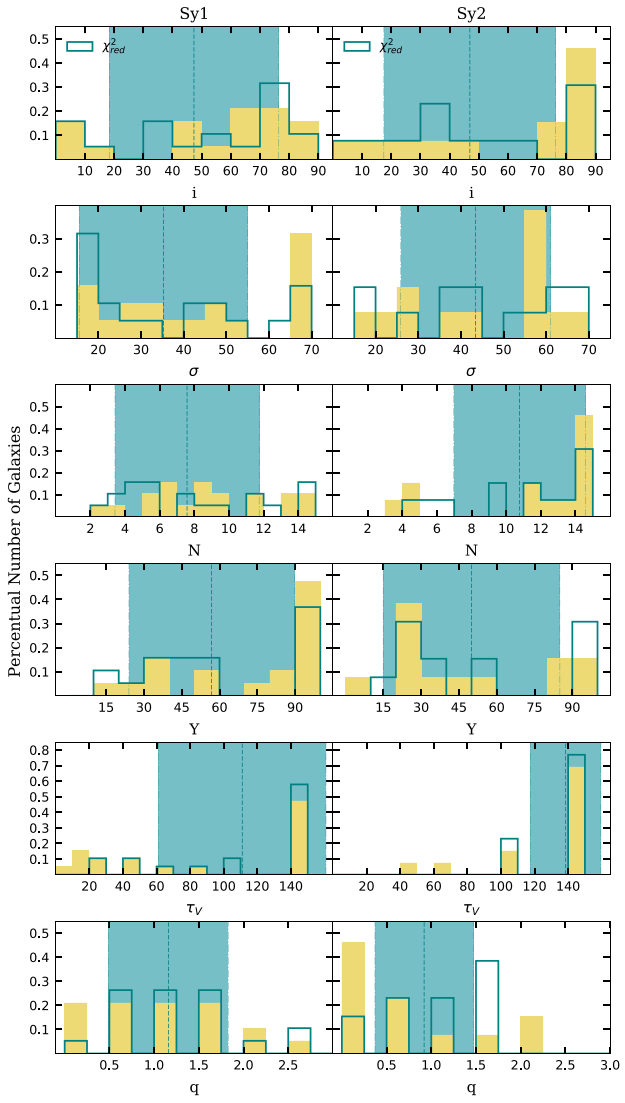

Figure 14. We present the histograms for the distribution of the direct parameters using both NIR+MIR spectra (stepped blue) and compared them with the analysis using the results for the 32 galaxies only considering the MIR data (yellow filled). The distributions for the 19 Sy 1 are plotted at the left side and for the 13 Sy 2 at the right side. The shaded areas indicate the mean values from the χ^2_{red} and the uncertainties around the average, represented by the dashed line, for the NIR+MIR combination.

and the torus properties is that usually data are not uniform. It is common to have a sample of sources in which the data are obtained with distinct filters and instruments (thus probing very different regions of the sources), and in some cases they do not have the same wavelength coverage for each individual galaxy. Consequently, this can lead to different results of the fitting (Ramos Almeida et al. 2014).

6 CONCLUSIONS

We proposed to investigate the torus properties in a sample of 46 Sy 1 and 65 Sy 2 galaxies in the unified model scenario. The sample consists of all 5–38 μm IRS/*Spitzer* data available in the heritage archive for Seyfert classification. To isolate the emission from the nucleus, we subtracted the host galaxy contribution in the MIR by removing the PAH band emission via an IRS spectral decomposing code (PAHFIT; Smith et al. 2007b).

Recently, many efforts have been made to calculate the torus emission in a clumpiness formalism. One of them is developed by Nenkova et al. (2008a,b, CLUMPY models), and here in this work we utilize their $\sim 10^6$ theoretical data base models to derive the six parameters that better adjust the individual MIR spectra and analyse their distribution.

We found differences in the derived mean values for the observers' viewing angle, $\bar{i} = 50^\circ$ for Sy 1 and $\bar{i} = 65^\circ$ for Sy 2, according to the unified model, which suggest that type 2 objects are observed mostly in edge-on angle views than type 1. Type 2 also appears to be angularly larger, with a mean Gaussian width distribution of $\sigma = 44$, while the Sy 1 class present $\bar{\sigma} = 36$ and a slightly larger mean torus thickness, $\bar{Y} = 54$ ($\bar{Y} = 46$ for Sy 2). Despite the fact that we found almost the same number of clouds along the equatorial ray, $N \sim 10$, the number of clouds obscuring the central source in the observer LOS is, on average, 7 for Sy 2 and $N_{los} \sim 4$ in Sy 1, indicating most attenuated SEDs from type 2 sources. The radial index power tends to be more like a flattened radial distribution, with $q \leq 1$ in the majority cases, while the τ_V distribution attends the criteria of $\tau_V \gtrsim 60$ for both types but does present higher values for Sy 2, ($\bar{\tau_V}$(Sy 1) = 7 and $\bar{\tau_V}$(Sy 2) = 111), indicating that the cloud physical properties may be distinct.

The obscuration in type 2 objects requires higher extinction values, with an average value of $A_V \sim 900$, while for Sy 1 the average found is ∼290. The torus masses range from $M_{tor} \sim 10^4$ to 10^7 M$_\odot$ in both cases. Properties are derived from the torus symmetry and random distribution nature, C_T and P_{esc}, where the P_{esc} parameter ensures non-zero AGN probabilities to edge-on inclination; we found about 30 per cent of probability to directly see the central source in type 1 and 10 per cent for Sy 2 in the sample. Geometric covering factors, or the probabilities of absorption by the torus, are in agreement with the prediction for Sy 2; we found that in general in 80 per cent of the cases the central source is obscured. However, the mean values derived for the Sy 1 ($C_T \sim 0.7$) are larger than the values found in previous works (e.g. AH11 and RA11).

We would like to highlight the importance of the use of a large and homogeneous sample in order to the determine in a reliable way the torus properties. In general, the inclusion of *JHK* spectroscopic data in our MIR sample does not change the global torus properties derived for each type of activity.

Finally, our results follow the orientation dependence suggested by unification schemes. However, some properties concerning the cloud obscuration are not intrinsically the same for both types of activity. The torus geometry and cloud properties, along with orientation effects, may be crucial to characterize the differences between Sy1 and Sy2, supporting the findings of RA11 and AH11.

On the basis of the presented results, the classification of a Seyfert galaxy may also depend on the dust intrinsic properties of the dusty torus clouds rather than only on the torus inclination angle, in contradiction with the simple geometrical requirements of the putative torus of the unification model.

ACKNOWLEDGEMENTS

We would like to thank the anonymous referee for useful comments that helped to improve the paper. AA and RR would like to acknowledge the financial support from CNPq during this project. DS would like to acknowledge the financial support from FAPERGS/CAPES.

This research has made use of the NASA/IPAC Extragalactic Database (NED) which is operated by the Jet Propulsion Laboratory, California Institute of Technology, under contract with the National Aeronautics and Space Administration. This work is based on observations made with the *Spitzer Space Telescope*, which is operated by the Jet Propulsion Laboratory, California Institute of Technology under a contract with NASA.

REFERENCES

Alonso-Herrero A. et al., 2011, ApJ, 736, 82 (AH11)
Antonucci R., 1993, ARA&A, 31, 473
Antonucci R. R. J., Miller J. S., 1985, ApJ, 297, 621
Asensio Ramos A., Ramos Almeida C., 2009, ApJ, 696, 2075
Asmus D., Gandhi P., Smette A., Hönig S. F., Duschl W. J., 2011, A&A, 536, A36
Barvainis R., 1987, ApJ, 320, 537
Begelman M. C., Blandford R. D., Rees M. J., 1984, Rev. Mod. Phys., 56, 255
Bohlin R. C., Savage B. D., Drake J. F., 1978, ApJ, 224, 132
Buchanan C. L., Gallimore J. F., O'Dea C. P., Baum S. A., Axon D. J., Robinson A., Elitzur M., Elvis M., 2006, AJ, 132, 401
Burtscher L., Jaffe W., Raban D., Meisenheimer K., Tristram K. R. W., Röttgering H., 2009, ApJ, 705, L53
Cid Fernandes R. et al., 2013, A&A, 557, A86
Dadina M., 2007, A&A, 461, 1209
Davies R., Burtscher L., Dodds-Eden K., Orban de Xivry G., 2012, J. Phys.: Conf. Ser., 372, 2046
Dullemond C. P., van Bemmel I. M., 2005, A&A, 436, 47
Efstathiou A., Rowan-Robinson M., 1995, MNRAS, 273, 649
Elitzur M., 2012, ApJ, 747, L33
Elvis M. et al., 1994, ApJS, 95, 1
Esquej P. et al., 2014, ApJ, 780, 86
Fritz J., Franceschini A., Hatziminaoglou E., 2006, MNRAS, 366, 767
Fuller L. et al., 2016, MNRAS, 462, 2618
Gallimore J. F. et al., 2010, ApJS, 187, 172
García-Burillo S. et al., 2014, A&A, 567, A125
García-Burillo S. et al., 2016, ApJ, 823, L12
González Delgado R. M., Heckman T., Leitherer C., 2001, ApJ, 546, 845
Granato G. L., Danese L., 1994, MNRAS, 268, 235
Gratadour D., Rouan D., Grosset L., Boccaletti A., Clénet Y., 2015, A&A, 581, L8
Hao L., Weedman D. W., Spoon H. W. W., Marshall J. A., Levenson N. A., Elitzur M., Houck J. R., 2007, ApJ, 655, L77
Hernán-Caballero A. et al., 2015, ApJ, 803, 109
Ho L. C., 2009, ApJ, 699, 626
Hönig S. F., Beckert T., Ohnaka K., Weigelt G., 2006, A&A, 452, 459
Houck J. R. et al., 2004, ApJS, 154, 18
Ichikawa K. et al., 2015, ApJ, 803, 57
Imanishi M., Nakanishi K., Izumi T., 2016 ApJ, 822, L10
Ivezic Z., Nenkova M., Elitzur M., 1999, User Manual for DUSTY. Univ. Kentucky Internal Report. Available at: http://www.pa.uky.edu/moshe/dusty
Jaffe W. et al., 2004, Nature, 429, 47
Kennicutt R. C. et al., 2003, PASP, 115, 928
Krolik J. H., Begelman M. C., 1988, ApJ, 329, 702
Lebouteiller V., Barry D. J., Spoon H. W. W., Bernard-Salas J., Sloan G. C., Houck J. R., Weedman D. W., 2011, ApJS, 196, 8
Lira P., Videla L., Wu Y., Alonso-Herrero A., Alexander D., Ward M., 2013, ApJ, 764, 59
López-Gonzaga N., Jaffe W., Burtscher L., Tristram K. R. W., Meisenheimer K., 2014, A&A, 565, A71
Lutz D., Maiolino R., Spoon H. W. W., Moorwood A. F. M., 2004, A&A, 418, 465
Lynden-Bell D., 1969, Nature, 223, 690
Maiolino R., Shemmer O., Imanishi M., Netzer H., Oliva E., Lutz D., Sturm E., 2007, A&A, 468, 979
Marinucci A., Bianchi S., Nicastro F., Matt G., Goulding A. D., 2012, ApJ, 748, 130
Mason R. E., Levenson N. A., Shi Y., Packham C., Gorjian V., Cleary K., Rhee J., Werner M., 2009, ApJ, 693, 136
Mason R. E. et al., 2015, ApJS, 217, 13
Mateos S. et al., 2016, ApJ, 819, 166
Mathis J. S., Rumpl W., Nordsieck K. H., 1977, ApJ, 217, 425
Mor R., Netzer H., Elitzur M., 2009, ApJ, 705, 298
Nenkova M., Ivezić Ž., Elitzur M., 2002, ApJ, 570, L9
Nenkova M., Sirocky M. M., Ivezić Ž., Elitzur M., 2008a, ApJ, 685, 147
Nenkova M., Sirocky M. M., Nikutta R., Ivezić Ž., Elitzur M., 2008b, ApJ, 685, 160
Netzer H., 2015, ARA&A, 53, 365
Nikutta R., Elitzur M., Lacy M., 2009, ApJ, 707, 1550
Pérez García A. M., Rodríguez Espinosa J. M., 2001, ApJ, 557, 39
Pier E. A., Krolik J. H., 1992, ApJ, 401, 99
Pogge R. W., 1988, ApJ, 328, 519
Raban D., Jaffe W., Röttgering H., Meisenheimer K., Tristram K., 2009, MNRAS, 394, 1325
Ramos Almeida C. et al., 2009, ApJ, 702, 1127 (RA09)
Ramos Almeida C. et al., 2011, ApJ, 731, 92 (RA11)
Ramos Almeida C., Alonso-Herrero A., Levenson N., Asensio Ramos A., Rodríguez Espinosa J. M., González-Martín O., Packham C., Martínez M., 2014, MNRAS, 439, 3847
Riffel R., Rodríguez-Ardila A., Pastoriza M. G., 2006, A&A, 457, 61
Riffel R., Pastoriza M. G., Rodríguez-Ardila A., Bonatto C., 2009, MNRAS, 400, 273
Rodríguez-Ardila A., Mazzaly Z., 2006, MNRAS, 367, L57
Rodríguez-Ardila A., Viegas S. M., 2003, MNRAS, 340, L33
Ruschel-Dutra D., Pastoriza M., Riffel R., Sales D. A., Winge C., 2014, MNRAS, 108
Sales D. A., Pastoriza M. G., Riffel R., 2010, ApJ, 725, 605
Sales D. A., Pastoriza M. G., Riffel R., Winge C., 2013, MNRAS, 429, 2634
Sales D. A., Ruschel-Dutra D., Pastoriza M. G., Riffel R., Winge C., 2014, MNRAS, 441, 630
Sanders D. B., Mazzarella J. M., Kim D. C., Surace J. A., Soifer B. T., 2003, AJ, 126, 1607
Schartmann M., Meisenheimer K., Camenzind M., Wolf S., Tristram K. R. W., Henning T., 2008, A&A, 482, 67
Siebenmorgen R., Krügel E., Spoon H. W. W., 2004, A&A, 414, 123
Smith J. D. T. et al., 2007a, PASP, 119, 1133
Smith J. D. T. et al., 2007b, ApJ, 656, 770
Stalevski M., Fritz J., Baes M., Nakos T., Popović L. Č., 2012, MNRAS, 420, 2756
Storchi-Bergmann T., Bonatto C. J., 1991, MNRAS, 250, 138
Storchi-Bergmann T., Wilson A. S., Baldwin J. A., 1992, ApJ, 396, 45
Sturm E., Hasinger G., Lehmann I., Mainieri V., Genzel R., Lehnert M. D., Lutz D., Tacconi L. J., 2006, ApJ, 642, 81
Tran H. D., 1995, ApJ, 440, 565
Tran H. D., Miller J. S., Kay L. E., 1992, ApJ, 397, 452
Tristram K. R. W. et al., 2007, A&A, 474, 837
Tristram K. R. W. et al., 2009, A&A, 502, 67
Tristram K. R. W., Burtscher L., Jaffe W., Meisenheimer K., Hönig S. F., Kishimoto M., Schartmann M., Weigelt G., 2014, A&A, 563, A82
Urry C. M., Padovani P., 1995, PASP, 107, 803
Vasudevan R. V., Fabian A. C., Gandhi P., Winter L. M., Mushotzky R. F., 2010, MNRAS, 402, 1081
von Mises R., 1964, Mathematical Theory of Probability and Statistics. Academic Press, New York
Whittle M., 1992, ApJS, 79, 49
Wu Y., Charmandaris V., Huang J., Spinoglio L., Tommasin S., 2009, ApJ, 701, 658

APPENDIX A: SAMPLE PROPERTIES

We present in Table A1 the main properties for our 111 Seyfert sample.

Table A1. Sample properties.

Object name	RA J2000	Dec. J2000	z	Distance (Mpc)	Morphological type	$\log(L_{IR})$ ($L_\odot$)	$L_{2-10\,keV}$ (erg s^{-1})	Active type	PID
Mrk 334[a]	$00^h03^m09\overset{s}{.}6$	$+21^d57^m37^s$	0.022	86.7	Pec	11.02[(2)]		Sy 1	3374
Mrk 335	$00^h06^m19\overset{s}{.}5$	$+20^d12^m10^s$	0.026	110.4	Compact	10.72[(1)]	9.75e+42[(6)]	Sy 1	3269
Mrk 938	$00^h11^m06\overset{s}{.}5$	$-12^d06^m26^s$	0.020	84.0	Pec	11.48[(1)]		Sy 2	3269
E12-G21	$00^h40^m46\overset{s}{.}1$	$-79^d14^m24^s$	0.030	128.6	E	11.03[(1)]		Sy 1	3269
Mrk 348[a]	$00^h48^m47\overset{s}{.}1$	$+31^d57^m25^s$	0.015	64.4	SA0/a	10.62[(1)]	2.47e+43[(8)]	Sy 2	3269
NGC 424	$01^h11^m27\overset{s}{.}6$	$-38^d05^m00^s$	0.012	50.4	SB0/a	10.67[(1)]		Sy 2	3269
NGC 526A	$01^h23^m54\overset{s}{.}4$	$-35^d03^m56^s$	0.019	81.8	S0 pec	10.78[(1)]	1.21e+43[(6)]	Sy 1	86, 3269
NGC 513	$01^h24^m26\overset{s}{.}8$	$+33^d47^m58^s$	0.020	83.7	Sb/c	10.52[(1)]	5.25e+42[(8)]	Sy 2	3269
Mrk 993[a]	$01^h25^m31\overset{s}{.}4$	$+32^d08^m11^s$	0.016	60.6	Sa	10.99[(4)]		Sy 1	40385
Mrk 573[a]	$01^h43^m57\overset{s}{.}8$	$+02^d21^m00^s$	0.017	67.4	SAB0	10.48[(2)]		Sy 2	50094
F01475-0740	$01^h50^m02\overset{s}{.}7$	$-07^d25^m48^s$	0.018	75.7	E/S0	10.62[(1)]	3.31e+43[(8)]	Sy 2	3269
NGC 931	$02^h28^m14\overset{s}{.}5$	$+31^d18^m42^s$	0.017	71.3	Sbc	10.92[(1)]		Sy 1	3269
NGC 1056	$02^h42^m48\overset{s}{.}3$	$+28^d34^m27^s$	0.005	22.1	Sa	9.93[(1)]		Sy 2	3269
NGC 1097[a]	$02^h46^m19\overset{s}{.}0$	$-30^d16^m30^s$	0.004	17.5	SBb	10.78[(1)]	7.59e+40[(9)]	Sy 2	159
NGC 1125	$02^h51^m40\overset{s}{.}3$	$-16^d39^m04^s$	0.011	46.8	SAB0	10.46[(1)]		Sy 2	3269
NGC 1143/4	$02^h55^m12\overset{s}{.}2$	$-00^d11^m01^s$	0.029	123.5	S0 pec	10.46[(1)]		Sy 2	159
Mrk 1066[a]	$02^h59^m58\overset{s}{.}6$	$+36^d49^m14^s$	0.012	47.2	SB0	10.78[(2)]	8.32e+42[(8)]	Sy 2	30572
M-2-8-39	$03^h00^m30\overset{s}{.}6$	$-11^d24^m57^s$	0.029	128	SABa pec	10.95[(1)]	7.94e+43[(11)]	Sy 2	3269
NGC 1194	$03^h03^m49\overset{s}{.}1$	$-01^d06^m13^s$	0.014	58.2	SA0:	10.34[(1)]	6.31e+43[(11)]	Sy 2	3269
NGC 1241	$03^h11^m14\overset{s}{.}6$	$-08^d55^m20^s$	0.014	57.9	SBb	10.75[(1)]		Sy 2	3269
NGC 1275[a]	$03^h19^m48\overset{s}{.}1$	$+41^d30^m42^s$	0.017	70.9	Pec	11.20[(5)]	7.24e+42[(10)]	Sy 2	14
NGC 1320	$03^h24^m48\overset{s}{.}7$	$-03^d02^m32^s$	0.009	37.7	S0/a	10.21[(1)]	4.90e+42[(8)]	Sy 2	159
Mrk 609	$03^h25^m25\overset{s}{.}3$	$-06^d08^m38^s$	0.034	143	ImPec		6.63e+42[(6)]	Sy 2	3374
NGC 1365	$03^h33^m36\overset{s}{.}4$	$-36^d08^m25^s$	0.005	17.7	SBb	11.23[(1)]	3.25e+41[(6)]	Sy 1	3269
NGC 1386	$03^h36^m46\overset{s}{.}2$	$-35^d59^m57^s$	0.003	16.2	Sa,S0	9.53[(1)]	6.16e+39[(6)]	Sy 2	3269
F03450+0055	$03^h47^m40\overset{s}{.}2$	$+01^d05^m14^s$	0.031	132.8	?	11.10[(1)]		Sy 1	3269
NGC 1566	$04^h20^m00\overset{s}{.}4$	$-54^d56^m16^s$	0.005	11.8	SABbc,Sc	10.61[(1)]	4.17e+41[(9)]	Sy 1	159
F04385-0828	$04^h40^m54\overset{s}{.}9$	$-08^d22^m22^s$	0.015	64.7	S0	10.82[(1)]	2.00e+43[(11)]	Sy 2	3269
NGC 1667	$04^h48^m37\overset{s}{.}1$	$-06^d19^m12^s$	0.015	65.0	SABc	11.02[(1)]	3.63e+42[(8)]	Sy 2	3269
E33-G2	$04^h55^m58\overset{s}{.}9$	$-75^d32^m28^s$	0.018	77.5	SB0	10.52[(1)]	4.35e+42[(6)]	Sy 2	3269
M-5-13-17[a]	$05^h19^m35\overset{s}{.}8$	$-32^d39^m28^s$	0.012	54.1	SB0/a,S0/a	10.28[(1)]		Sy 1	3269
Mrk 3	$06^h15^m36\overset{s}{.}3$	$+71^d02^m15^s$	0.0135	55.9	E2 pec	10.78[(2)]	2.32e+42[(6)]	Sy 2	14
Mrk 6	$06^h52^m12\overset{s}{.}2$	$+74^d25^m37^s$	0.019	80.6	SAB0:,Sa	10.63[(1)]	2.05e+43	[(6)] Sy 1	3269
ESO 428-G014[a]	$07^h16^m31\overset{s}{.}2$	$-29^d19^m29^s$	0.006	26	SAB0 pec			Sy 2	30572
Mrk 9	$07^h36^m57\overset{s}{.}0$	$+58^d46^m13^s$	0.040	170	S0: pec,SB	11.15[(1)]		Sy 1	3269
Mrk 79	$07^h42^m32\overset{s}{.}8$	$+49^d48^m35^s$	0.022	95	SBb,SBc	10.90[(1)]	2.51e+43[(12)]	Sy 1	3269
Mrk 78	$07^h42^m41\overset{s}{.}7$	$+65^d10^m37^s$	0.037	158	SB	11.04[(2)]		Sy 2	50094
Mrk 622	$08^h07^m41\overset{s}{.}0$	$+39^d00^m15^s$	0.023	99.6	S0			Sy 2	3374
NGC 2622	$08^h38^m10\overset{s}{.}9$	$+24^d53^m43^s$	0.029	124	SBb			Sy 1	3374
NGC 2639[b]	$08^h43^m38\overset{s}{.}1$	$+50^d12^m20^s$	0.011	47.7	SAa	10.34[(1)]	7.08e+40[(10)]	Sy 1	3269
Mrk 704	$09^h18^m26\overset{s}{.}0$	$+16^d18^m19^s$	0.029	125.2	SBa	10.97[(1)]		Sy 1	3269
NGC 2992	$09^h45^m42\overset{s}{.}0$	$-14^d19^m35^s$	0.008	30.5	Sa pec	10.51[(1)]	7.20e+41[(6)]	Sy 1	3269
Mrk 1239[a]	$09^h52^m19\overset{s}{.}1$	$-01^d36^m43^s$	0.0199	85.3	E-S0	10.86[(1)]		Sy 1	3269
NGC 3079[b]	$10^h01^m57\overset{s}{.}8$	$+55^d40^m47^s$	0.004	19.7	SBc	10.62[(1)]	1.05e+42[(8)]	Sy 2	3269
NGC 3227[a]	$10^h23^m30\overset{s}{.}6$	$+19^d51^m54^s$	0.004	20.9	SABa pec	9.97[(1)]	2.51e+42[(7)]	Sy 1	668, 3269
Mrk 34	$10^h34^m08\overset{s}{.}6$	$+60^d01^m52^s$	0.051	218	Sa	11.15[(2)]		Sy 2	50094
NGC 3511	$11^h03^m23\overset{s}{.}8$	$-23^d05^m12^s$	0.004	14.6	SAc	9.95[(1)]		Sy 1	3269
NGC 3516	$11^h06^m47\overset{s}{.}5$	$+72^d34^m07^s$	0.009	38.9	SB0	10.17[(1)]	3.77e+42[(6)]	Sy 1	3269
M+0-29-23	$11^h21^m12\overset{s}{.}2$	$-02^d59^m03^s$	0.025	106.6	SABb	11.36[(1)]		Sy 2	3269
NGC 3660	$11^h23^m32\overset{s}{.}3$	$-08^d39^m31^s$	0.012	52.6	SBbc	10.47[(1)]	7.94e+42[(11)]	Sy 2	3269
NGC 3786	$11^h39^m42\overset{s}{.}5$	$+31^d54^m33^s$	0.009	40.9	SABa/Pec			Sy 2	3374
NGC 3982	$11^h56^m28\overset{s}{.}1$	$+55^d07^m31^s$	0.004	21.8	SABb	9.81[(1)]	1.41e+41[(8)]	Sy 2	3269
NGC 4051[a]	$12^h03^m09\overset{s}{.}6$	$+44^d31^m53^s$	0.002	17.0	SABbc	9.66[(1)]	1.64e+40[(6)]	Sy 1	3269
UGC 7064	$12^h04^m43\overset{s}{.}3$	$+31^d10^m38^s$	0.025	107.1	SAB	11.18[(1)]		Sy 1	3269
NGC 4151[a]	$12^h10^m32\overset{s}{.}6$	$+39^d24^m21^s$	0.003	20.3	SABab	9.95[(1)]	2.42e+42[(6)]	Sy 1	3269
NGC 4235[b]	$12^h17^m09\overset{s}{.}9$	$+07^d11^m30^s$	0.008	38	SAa	10.30[(4)]	4.07e+41[(9)]	Sy 1	40936
Mrk 766[a]	$12^h18^m26\overset{s}{.}5$	$+29^d48^m46^s$	0.013	55.4	SBa	10.67[(1)]	6.44e+42[(6)]	Sy 1	3269

Table A1 – *continued*

Object name	RA J2000	Dec. J2000	z	Distance (Mpc)	Morphological type	$\log(L_{IR})$ ($L_\odot$)	$L_{2-10\,keV}$ (erg s^{-1})	Active type	PID
NGC 4388[b]	$12^h25^m46\overset{s}{.}7$	$+12^d39^m44^s$	0.008	18.1	SAb	10.73[(1)]	3.37e+42[(6)]	Sy 2	3269
NGC 4501	$12^h31^m59\overset{s}{.}2$	$+14^d25^m14^s$	0.008	20.7	SAb	10.98[(1)]	7.76e+38[(10)]	Sy 2	3269
NGC 4507	$12^h35^m36\overset{s}{.}6$	$-39^d54^m33^s$	0.012	53	SABab		4.70e+42[(6)]	Sy 2	30572
NGC 4579[b]	$12^h37^m43\overset{s}{.}5$	$+11^d49^m05^s$	0.005	16.8	SABc	10.17[(1)]	2.66e+41[(6)]	Sy 1	159
NGC 4593	$12^h39^m39\overset{s}{.}4$	$-05^d20^m39^s$	0.009	44.0	SBb	10.35[(1)]	5.74e+42[(6)]	Sy 1	3269
NGC 4594[b]	$12^h39^m59\overset{s}{.}4$	$-11^d37^m23^s$	0.003	10.9	SAa	9.75[(1)]	9.77e+39[(9)]	Sy 1	159
NGC 4602	$12^h40^m36\overset{s}{.}8$	$-05^d07^m59^s$	0.008	34.4	SABbc	10.44[(1)]		Sy 1	3269
Tol1238-364	$12^h40^m52\overset{s}{.}8$	$-36^d45^m21^s$	0.011	46.8	SBbc	10.87[(1)]		Sy 2	3269
M-2-33-34	$12^h52^m12\overset{s}{.}4$	$-13^d24^m53^s$	0.015	62.7	Sa	10.49[(1)]		Sy 1	3269
NGC 4941	$13^h04^m13\overset{s}{.}1$	$-05^d33^m06^s$	0.004	13.8	SABab	9.39[(1)]	2.71e+40[(6)]	Sy 2	86, 3269
NGC 4968	$13^h07^m06\overset{s}{.}0$	$-23^d40^m37^s$	0.010	42.2	SAB0	10.39[(1)]		Sy 2	3269
NGC 5005[b]	$13^h10^m56\overset{s}{.}2$	$+37^d03^m33^s$	0.003	17.5	SABbc	10.20[(1)]	8.71e+39[(10)]	Sy 2	3269
NGC 5033[b]	$13^h13^m27\overset{s}{.}5$	$+36^d35^m38^s$	0.003	20.6	SAc	10.05[(1)]	5.01e+40[(10)]	Sy 1	159
NGC 5135	$13^h25^m44\overset{s}{.}0$	$-29^d50^m01^s$	0.014	58.6	SBab	11.27[(1)]	1.26e+43[(7)]	Sy 2	3269
M-6-30-15	$13^h35^m53\overset{s}{.}8$	$-34^d17^m44^s$	0.008	33.2	S?	9.98[(1)]	6.22e+42[(6)]	Sy 1	3269
NGC 5256	$13^h38^m17\overset{s}{.}5$	$+48^d16^m37^s$	0.028	117.3	Pec	11.51[(1)]		Sy 2	3269
I4329A	$13^h49^m19\overset{s}{.}2$	$-30^d18^m34^s$	0.016	68.8	SA0	10.97[(1)]	7.42e+43[(6)]	Sy 1	3269
Mrk 279[a]	$13^h53^m03\overset{s}{.}4$	$+69^d18^m30^s$	0.030	129	S0	11.90[(4)]	6.31e+43[(12)]	Sy 1	666
NGC 5347	$13^h53^m17\overset{s}{.}8$	$+33^d29^m27^s$	0.008	36.7	SBab	10.04[(1)]	2.51e+42[(7)]	Sy 2	3269
Mrk 463E	$13^h56^m02\overset{s}{.}9$	$+18^d22^m19^s$	0.050	217	S pec	11.70[(2)]	1.86e+42[(6)]	Sy 2	105
NGC 5506	$14^h13^m14\overset{s}{.}8$	$-03^d12^m27^s$	0.006	28.7	Sa pec	10.44[(1)]	4.99e+42[(6)]	Sy 2	3269
NGC 5548[a]	$14^h17^m59\overset{s}{.}5$	$+25^d08^m12^s$	0.017	73.6	SA0/a	10.66[(1)]	1.95e+43[(6)]	Sy 1	86, 3269
Mrk 471	$14^h22^m55\overset{s}{.}4$	$+32^d51^m03^s$	0.034	147	SBa			Sy 2	3374
Mrk 817	$14^h36^m22\overset{s}{.}1$	$+58^d47^m39^s$	0.031	134.7	SBc	11.35[(1)]		Sy 1	3269
NGC 5695	$14^h37^m22\overset{s}{.}1$	$+36^d34^m04^s$	0.014	60.7	SBb			Sy 2	30773
Mrk 477	$14^h40^m38\overset{s}{.}1$	$+53^d30^m16^s$	0.038	161	Comp	11.18[(2)]		Sy 2	30443
Mrk 478[a]	$14^h42^m07\overset{s}{.}4$	$+35^d26^m23^s$	0.079	347	S	11.37[(3)]	5.16e+43[(6)]	Sy 1	3187, 20142
NGC 5728[a]	$14^h42^m23\overset{s}{.}9$	$-17^d15^m11^s$	0.009	41.9	SABa	10.60[(5)]	1.95e+43[(8)]	Sy 2	30745
Mrk 841	$15^h04^m01\overset{s}{.}2$	$+10^d26^m16^s$	0.036	157	E	11.82[(4)]	3.27e+43[(6)]	Sy 1	14
NGC 5929[a]	$15^h26^m06\overset{s}{.}1$	$+41^d40^m14^s$	0.008	38.5	Sab pec	10.58[(1)]		Sy 2	3269
NGC 5953[a]	$15^h34^m32\overset{s}{.}4$	$+15^d11^m38^s$	0.007	33.0	SAa pec	10.49[(1)]		Sy 2	3269
M-2-40-4	$15^h48^m24\overset{s}{.}9$	$-13^d45^m28^s$	0.025	107.9	Sc	11.32[(1)]		Sy 2	3269
F15480-0344	$15^h50^m41\overset{s}{.}5$	$-03^d53^m18^s$	0.030	129.8	S0	11.14[(1)]		Sy 2	3269
Mrk 883	$16^h29^m52\overset{s}{.}9$	$+24^d26^m38^s$	0.037	159	Irr			Sy 2	3374
NGC 6810	$19^h43^m34\overset{s}{.}4$	$-58^d39^m21^s$	0.007	29.0	SAab	10.74[(1)]		Sy 2	3269
NGC 6860	$20^h08^m46\overset{s}{.}9$	$-61^d06^m01^s$	0.015	63.7	SBb	10.35[(1)]	3.98e+42[(12)]	Sy 1	3269
NGC 6890	$20^h18^m18\overset{s}{.}1$	$-44^d48^m25^s$	0.008	31.8	SAb	10.27[(1)]		Sy 2	3269
Mrk 509[a]	$20^h44^m09\overset{s}{.}7$	$-10^d43^m25^s$	0.034	48.6	Compact	11.21[(1)]	9.24e+43[(6)]	Sy 1	86
IC 5063	$20^h52^m02\overset{s}{.}3$	$-57^d04^m08^s$	0.011	48.6	SA0	10.87[(1)]	6.76e+42[(8)]	Sy 2	86, 3269
UGC 11680	$21^h07^m43\overset{s}{.}6$	$+03^d52^m30^s$	0.026	111.3	Scd	11.23[(1)]		Sy 2	3269
NGC 7130	$21^h48^m19\overset{s}{.}5$	$-34^d57^m05^s$	0.016	69.2	Sa pec	11.38[(1)]	1.26e+43[(7)]	Sy 2	3269
NGC 7172	$22^h02^m01\overset{s}{.}9$	$-31^d52^m11^s$	0.009	33.9	Sa pec	10.47[(1)]	1.65e+42[(6)]	Sy 2	86, 3269
NGC 7213	$22^h09^m16\overset{s}{.}2$	$-47^d10^m00^s$	0.006	22.0	SAa	10.01[(1)]	2.24e+42[(6)]	Sy 1	3269
NGC 7314	$22^h35^m46\overset{s}{.}2$	$-26^d03^m01^s$	0.005	19.0	SABbc	10.00[(1)]	1.13e+42[(6)]	Sy 1	86, 3269
M-3-58-7	$22^h49^m37\overset{s}{.}1$	$-19^d16^m26^s$	0.031	134.7	SAB0/a	11.30[(1)]	7.94e+43[(11)]	Sy 2	3269
NGC 7469[a]	$23^h03^m15\overset{s}{.}6$	$+08^d52^m26^s$	0.016	69.9	SABa	11.65[(1)]	1.86e+43[(6)]	Sy 1	3269
NGC 7496	$23^h09^m47\overset{s}{.}3$	$-43^d25^m41^s$	0.006	20.1	SBb	10.28[(1)]		Sy 2	3269
NGC 7582	$23^h18^m23\overset{s}{.}5$	$-42^d22^m14^s$	0.005	18.8	SBab	10.91[(1)]	1.01e+42[(6)]	Sy 2	3269
NGC 7590	$23^h18^m54\overset{s}{.}8$	$-42^d14^m21^s$	0.005	23.7	SAbc	10.19[(1)]	5.89e+39[(9)]	Sy 2	3269
NGC 7603	$23^h18^m56\overset{s}{.}6$	$+00^d14^m38^s$	0.030	126.4	SAb pec	11.05[(1)]		Sy 1	3269
NGC 7674[a]	$23^h27^m56\overset{s}{.}7$	$+08^d46^m45^s$	0.029	123.9	SAbc pec	11.57[(1)]	1.90e+42[(6)]	Sy 2	3269
NGC 7679	$23^h28^m46\overset{s}{.}7$	$+03^d30^m41^s$	0.017	66.2	SB0pec	11.05[(2)]	3.39e+42[(6)]	Sy 2	30323
NGC 7682*a*	$23^h29^m03\overset{s}{.}9$	$+03^d32^m00^s$	0.017	66.2	SBab	11.02[(4)]		Sy 2	50588
CGCG381-051	$23^h48^m41\overset{s}{.}7$	$+02^d14^m23^s$	0.031	131.3	SBc	11.19[(1)]		Sy 2	3269

[a]SpeX spectra available from Riffel et al. (2006, 2009).

[b]GNIRS spectra from Mason et al. (2015).

References: (1) Wu et al. (2009), (2) Gonzáles Delgado, Heckman & Leitherer (2001), (3) Rodríguez-Ardila & Viegas (2003), (4) Pérez García & Rodríguez Espinosa (2001), (5) Sanders et al. (2003), (6) Dadina (2007), (7) Esquej et al. (2014), (8) Marinucci et al. (2012), (9) Asmus et al. (2011), (10) Ho (2009), (11) Lira et al. (2013), (12) Vasudevan et al. (2010).

APPENDIX B: INDIVIDUAL SUBTRACTION

In this appendix, we present the individual results of the spectral decomposition and the subtracted spectra for each galaxy in our sample.

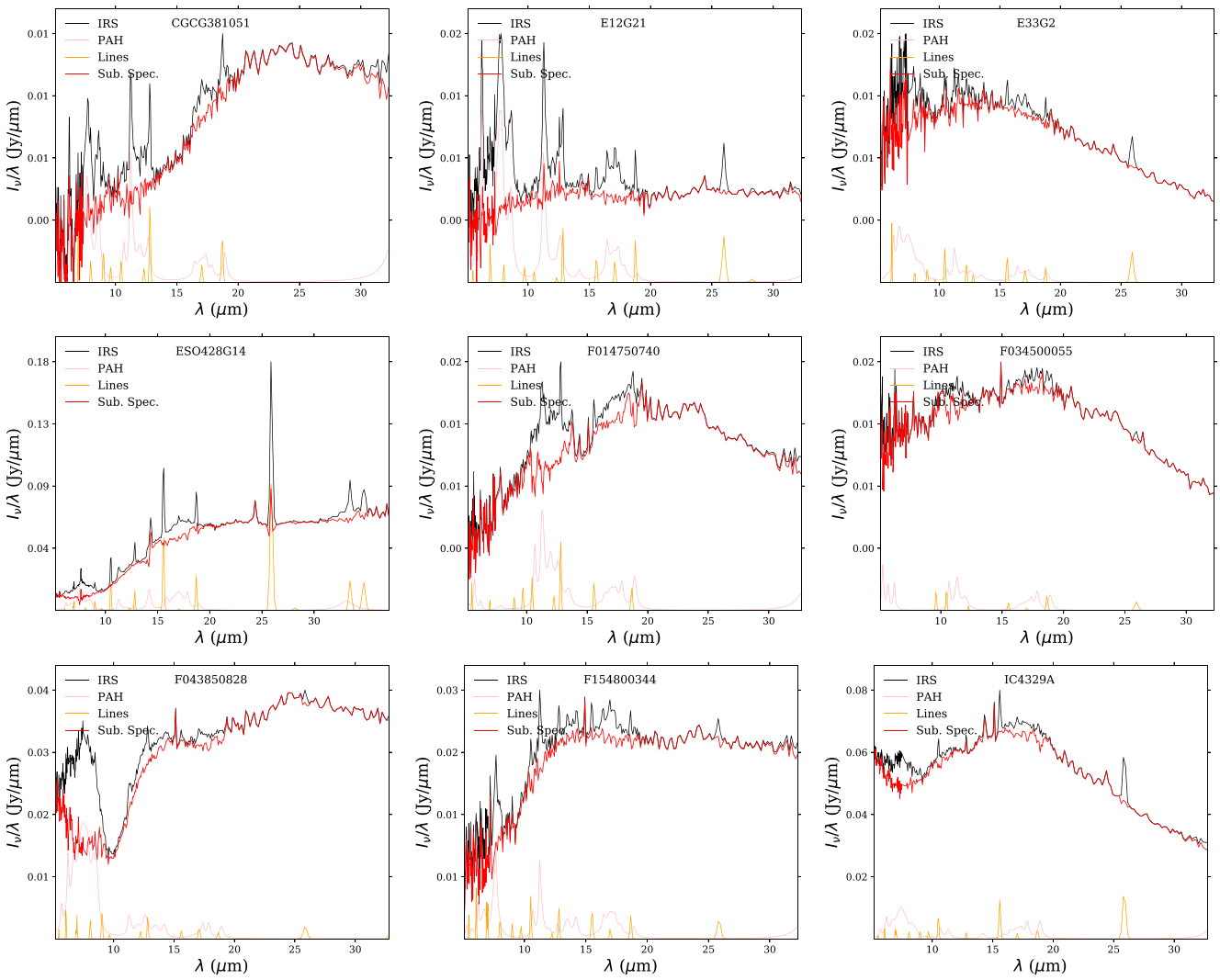

Figure B1. Individual spectral decomposition. We present the subtraction of the PAH and ionic line emission from the spectra. The black lines represent the observed IRS spectra, while the orange and pink lines show the resulting adjustments by fitting the PAH emission and ionic and hydrogen lines, respectively, using the PAHFIT (Smith et al. 2007b). In red are shown the subtracted spectra that were adopted in our analysis.

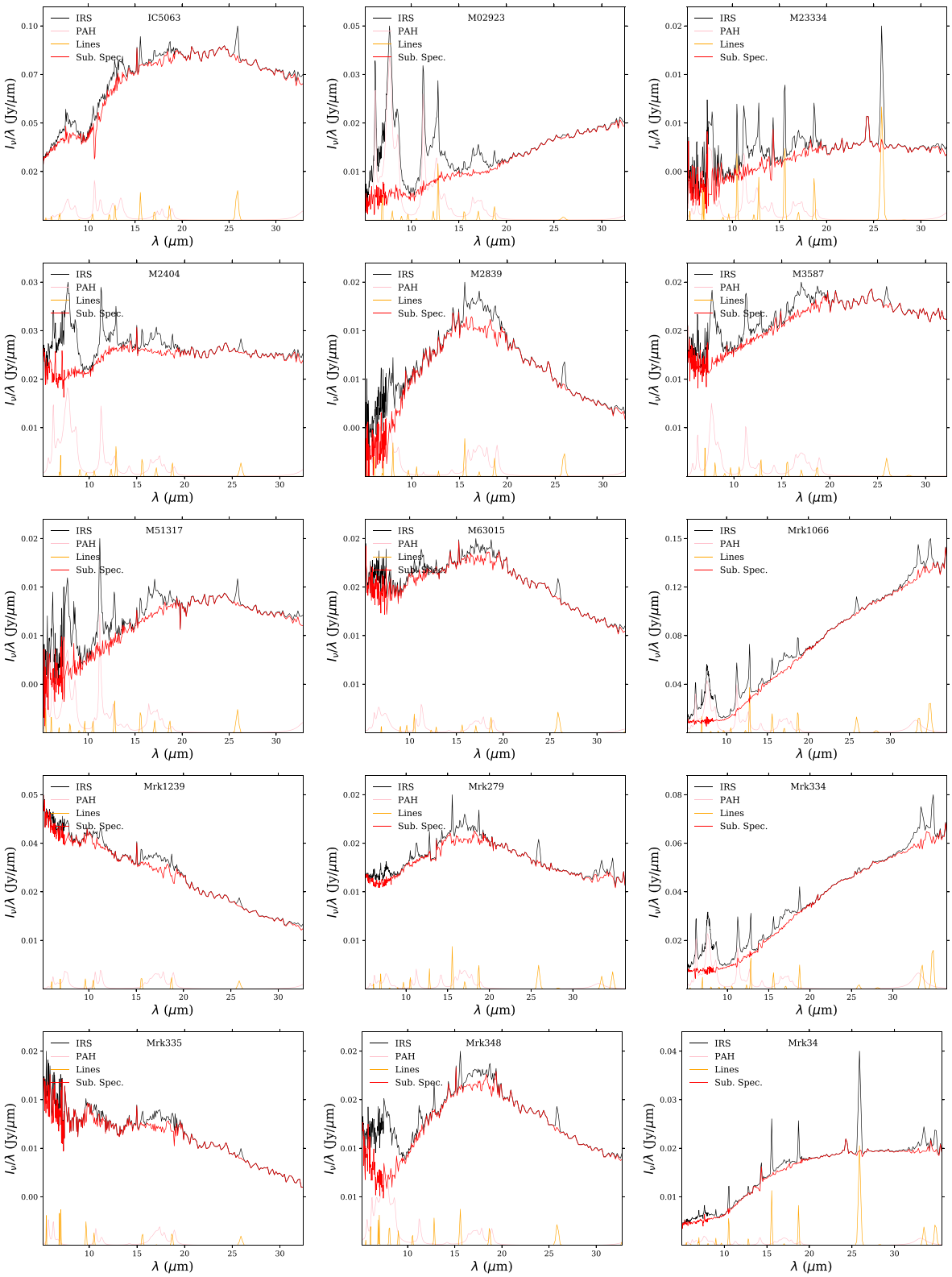

Figure B1 – *continued*

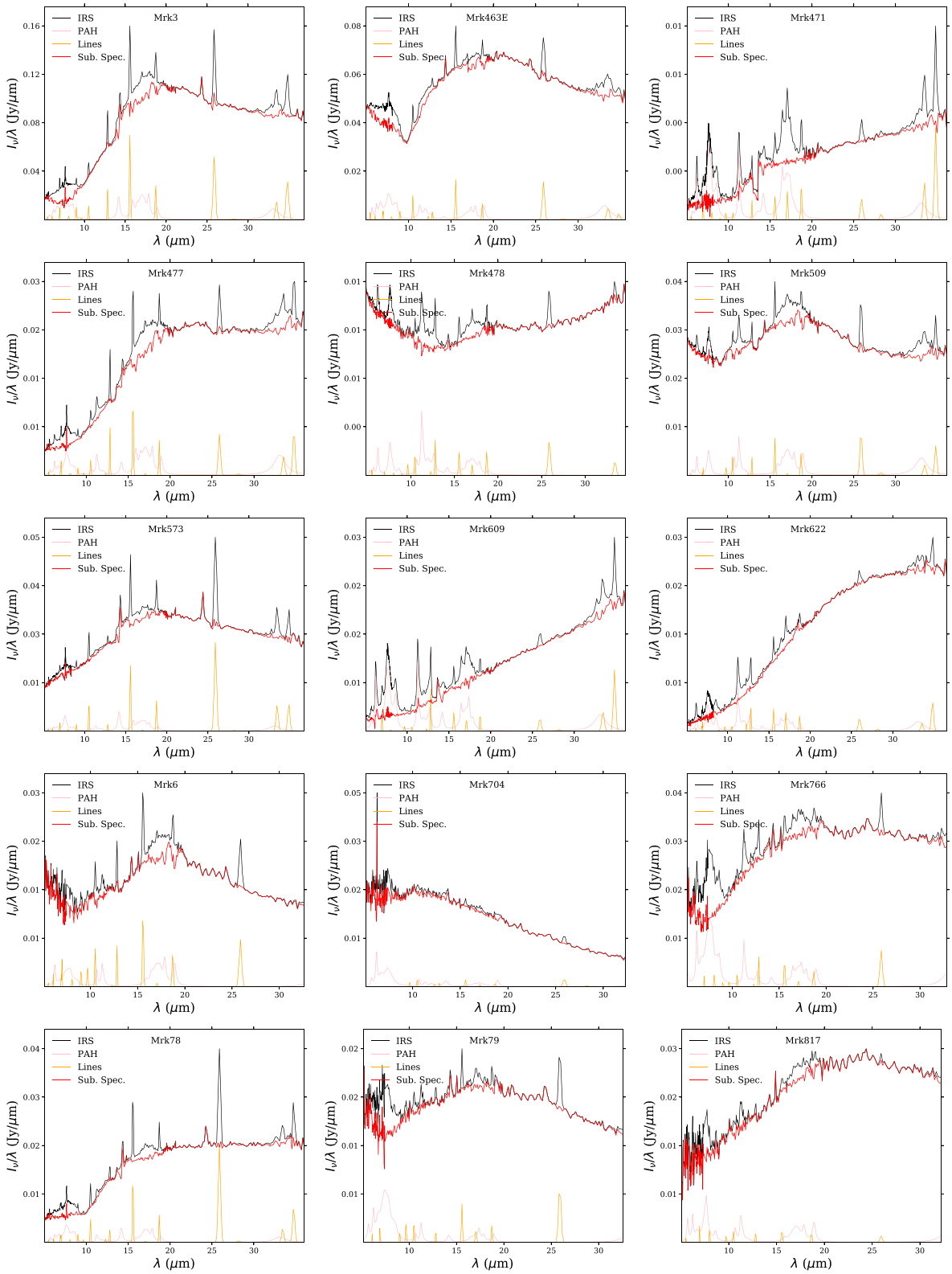

Figure B1 – *continued*

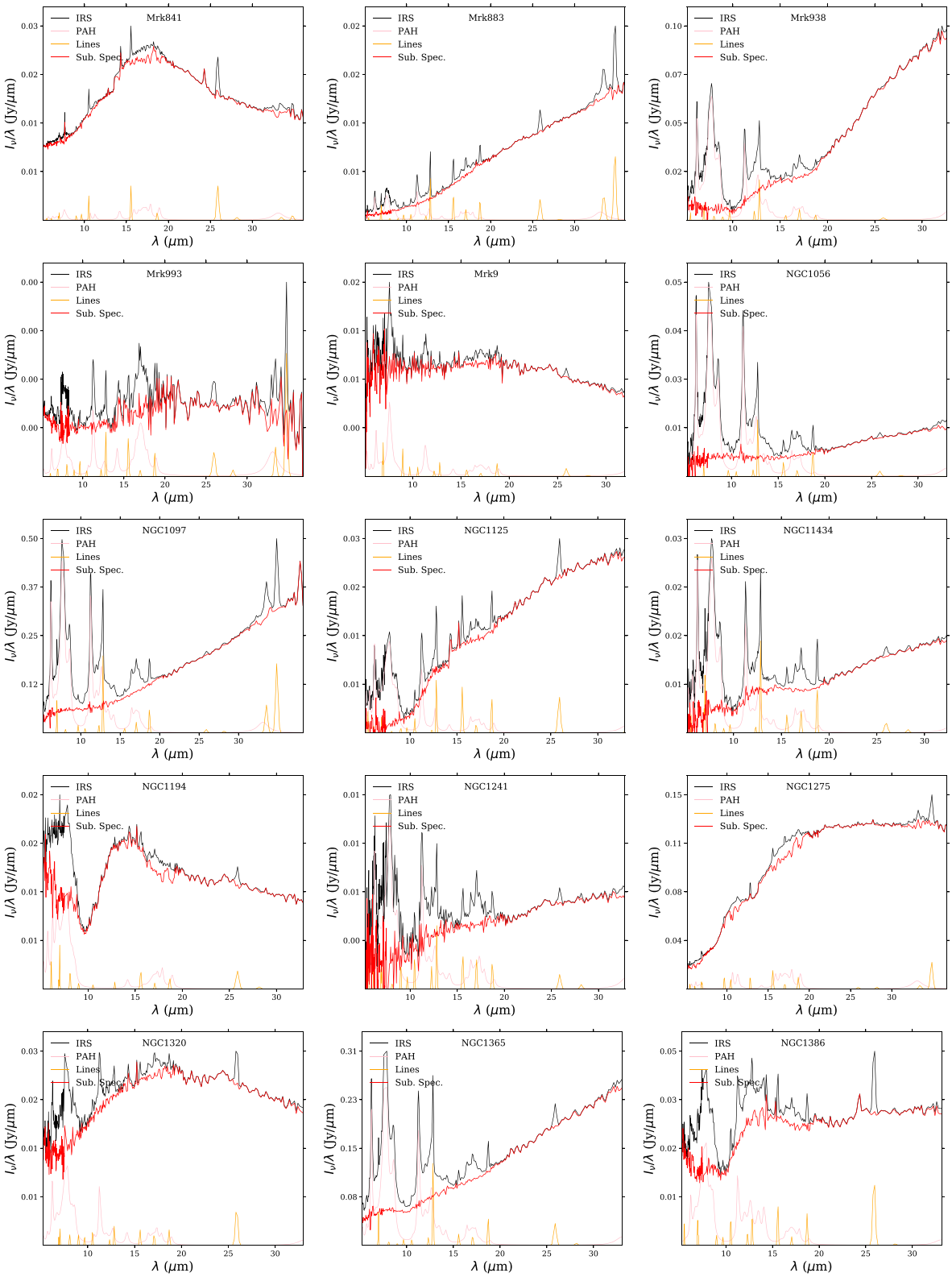

Figure B1 – *continued*

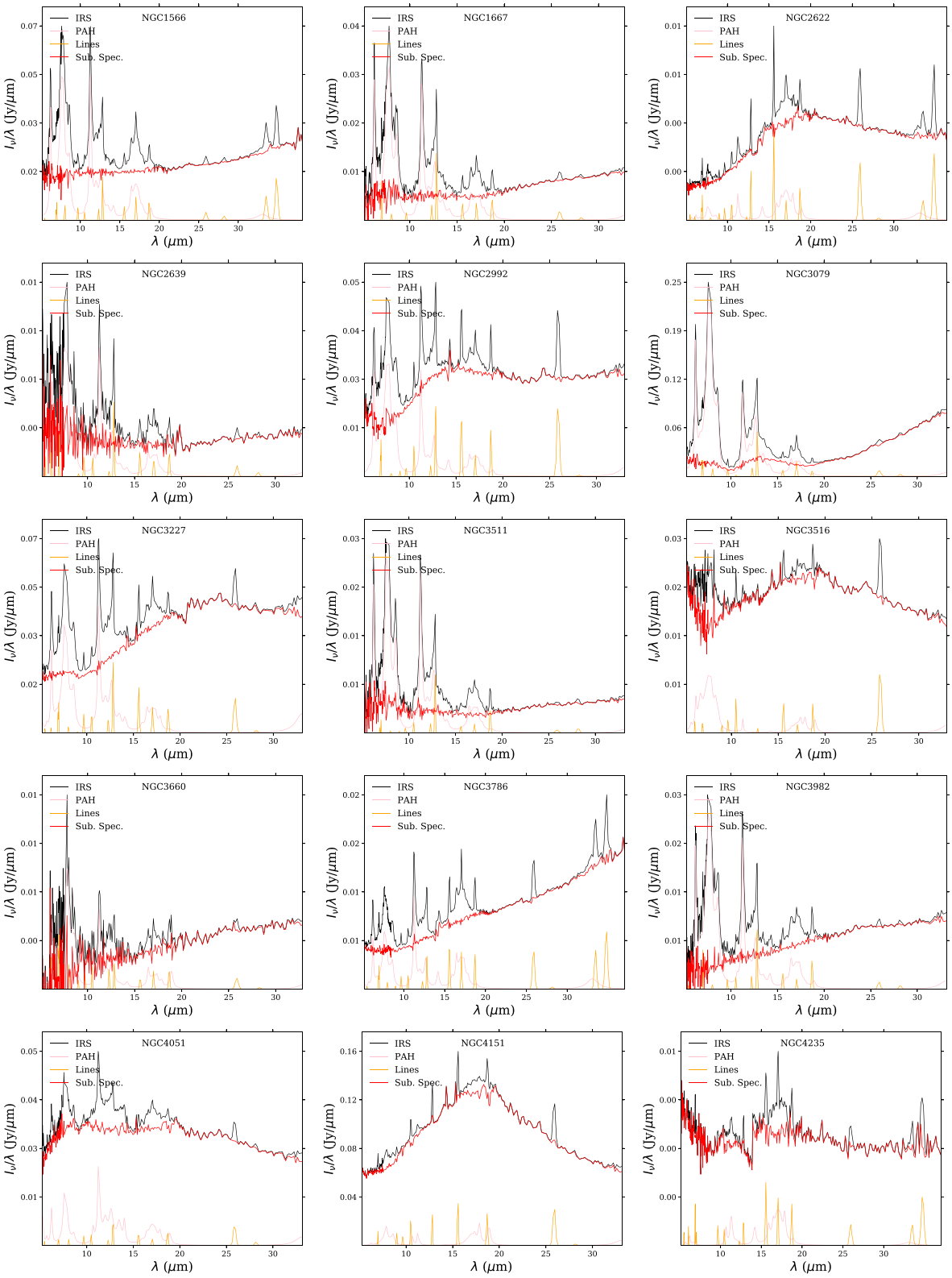

Figure B1 – *continued*

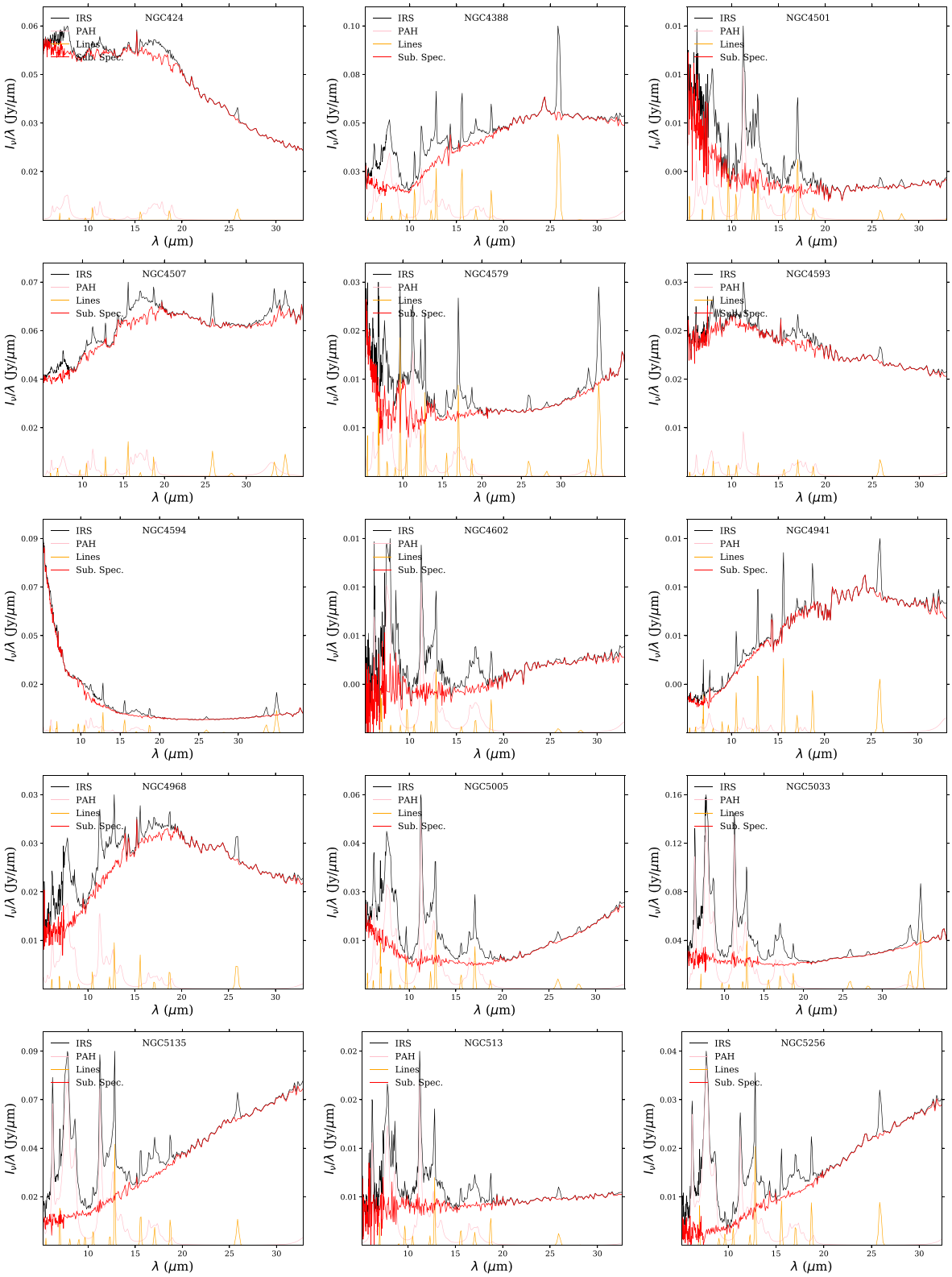

Figure B1 – *continued*

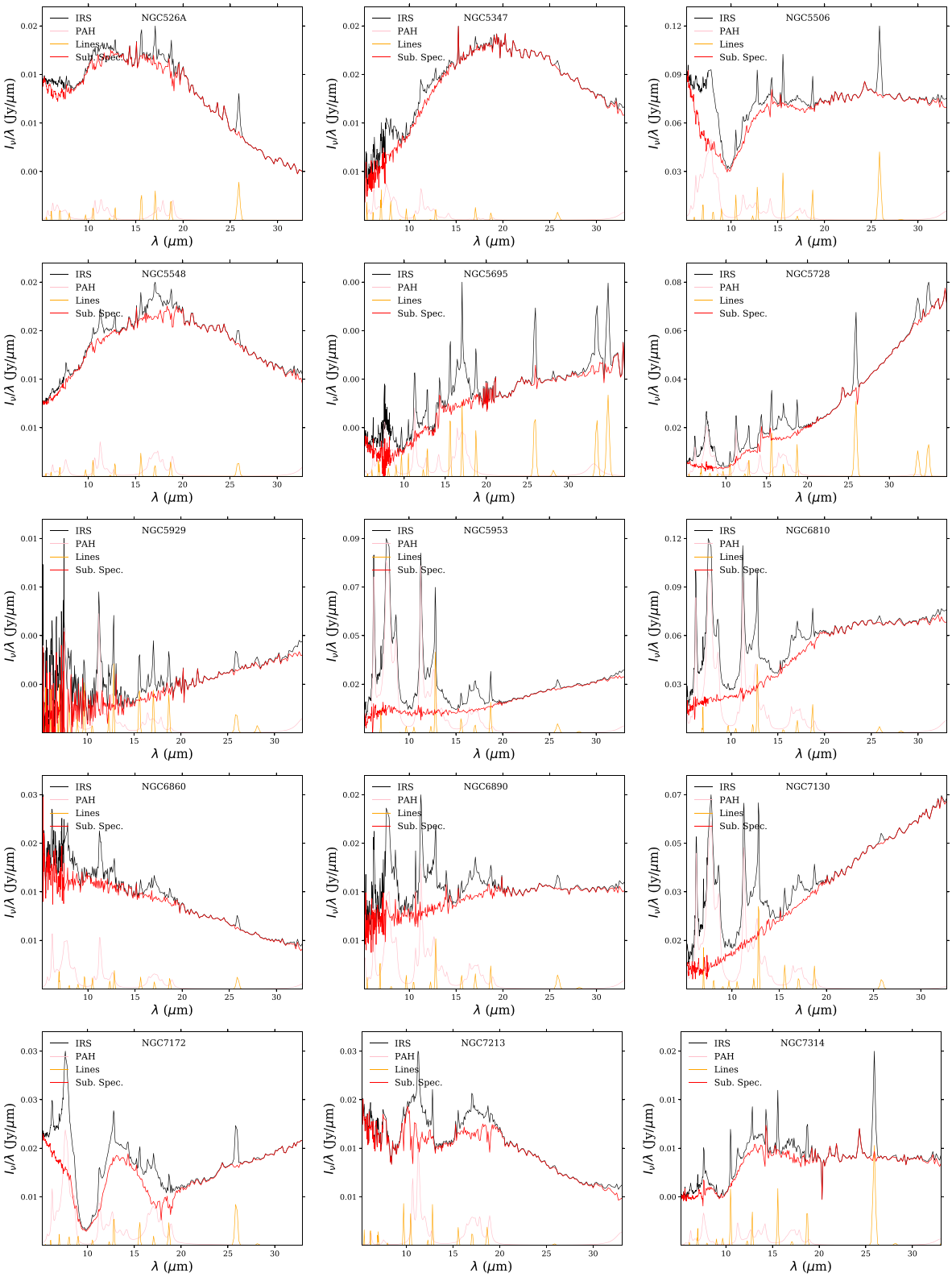

Figure B1 – *continued*

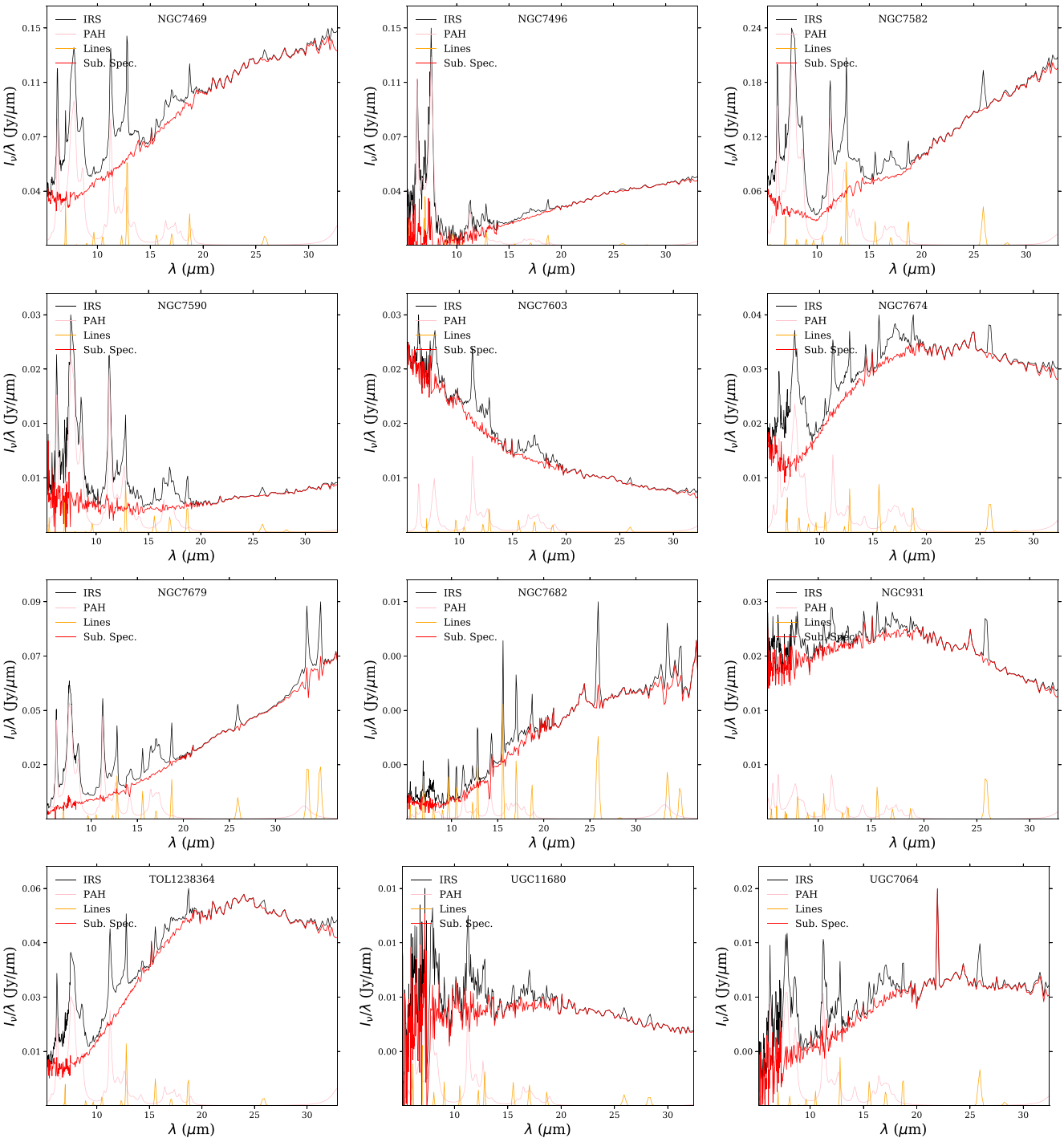

Figure B1 – *continued*

APPENDIX C: INDIVIDUAL ADJUSTMENTS

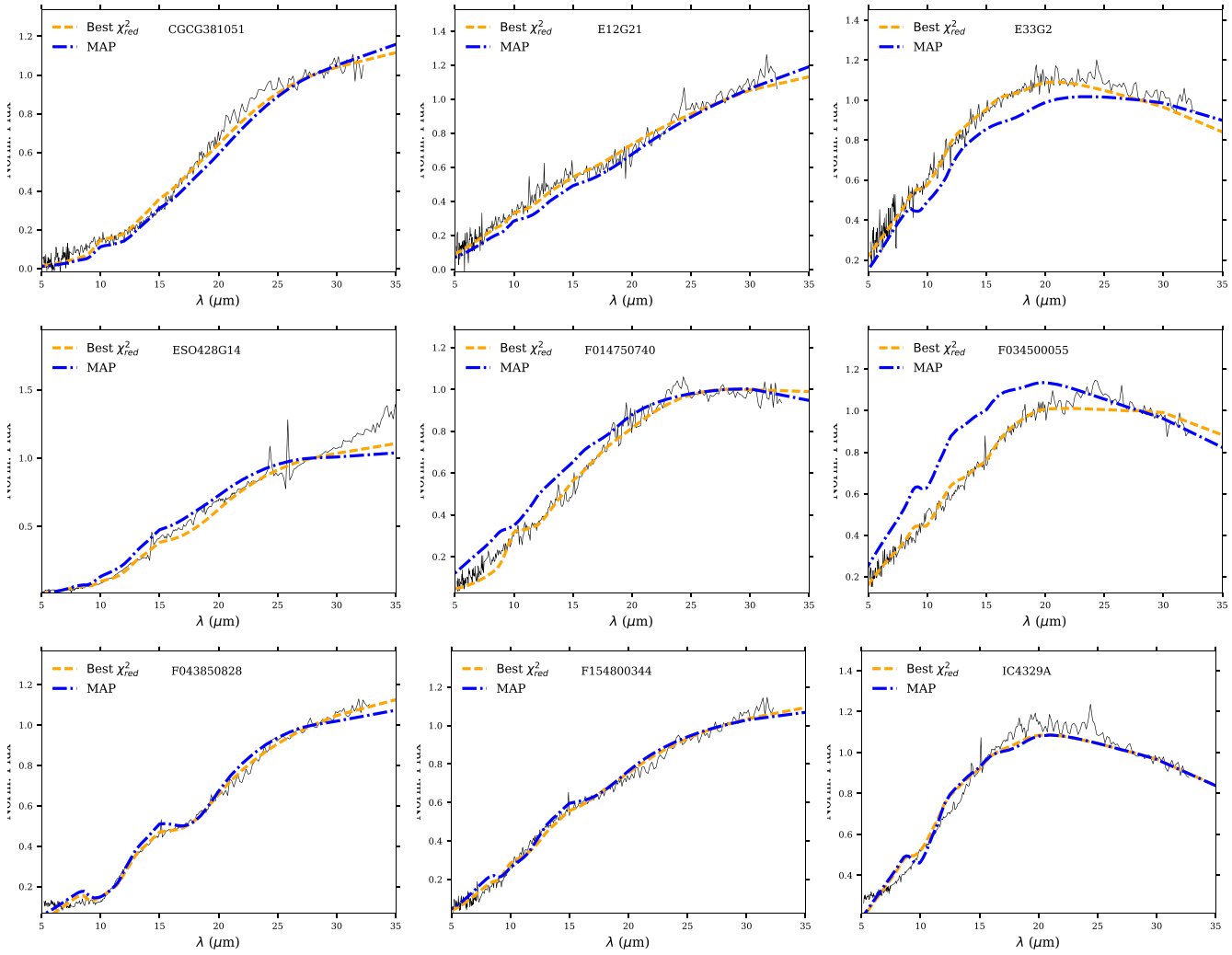

Figure C1. Individual fitting results. We present the adjustments for the best fit using $\chi^2_{\rm red}$ (yellow dashed line) and the MAP (blue dot–dashed line) distribution from BayesCLUMPY. The observed spectra and the SED models are normalized at 28 μm.

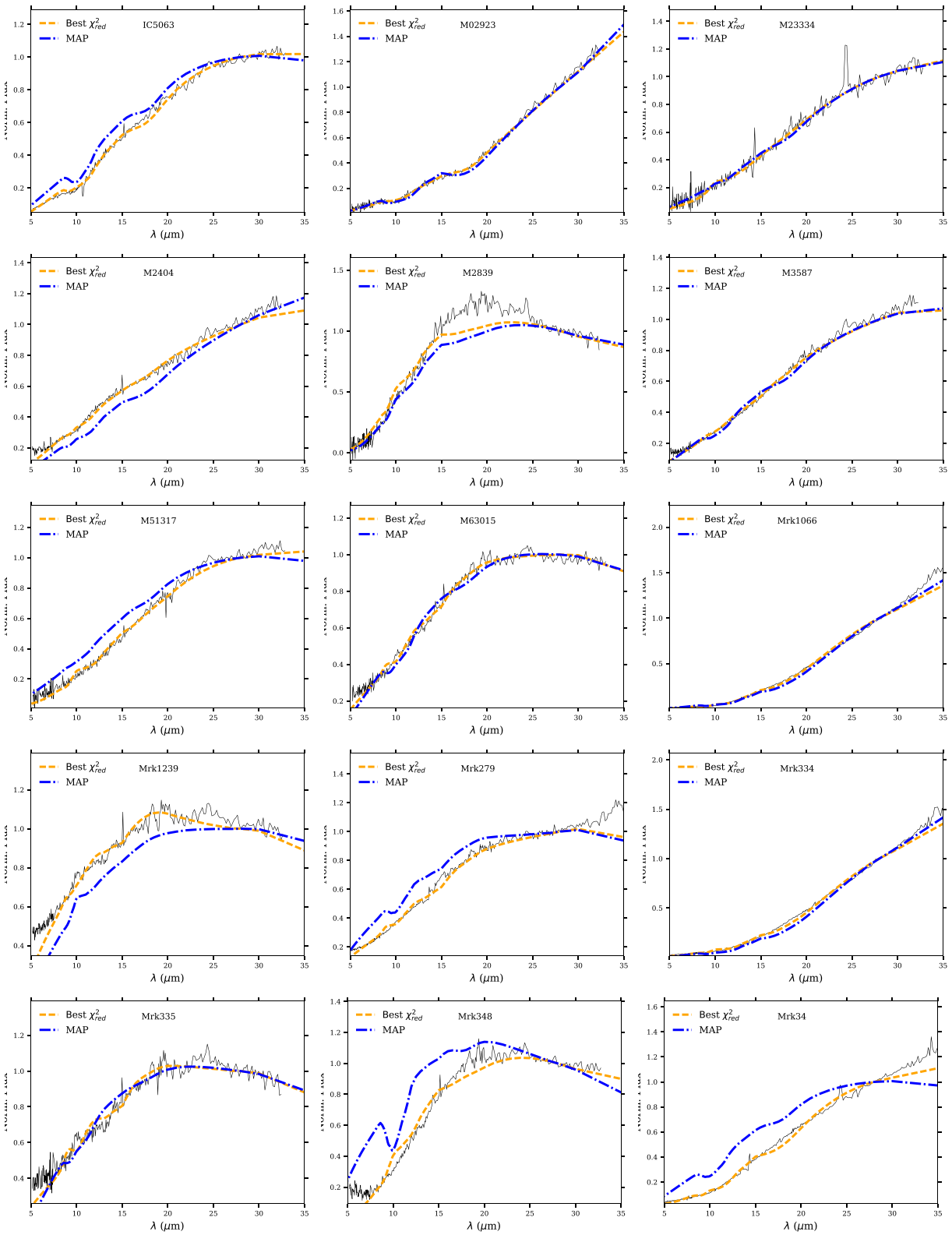

Figure C1 – *continued*

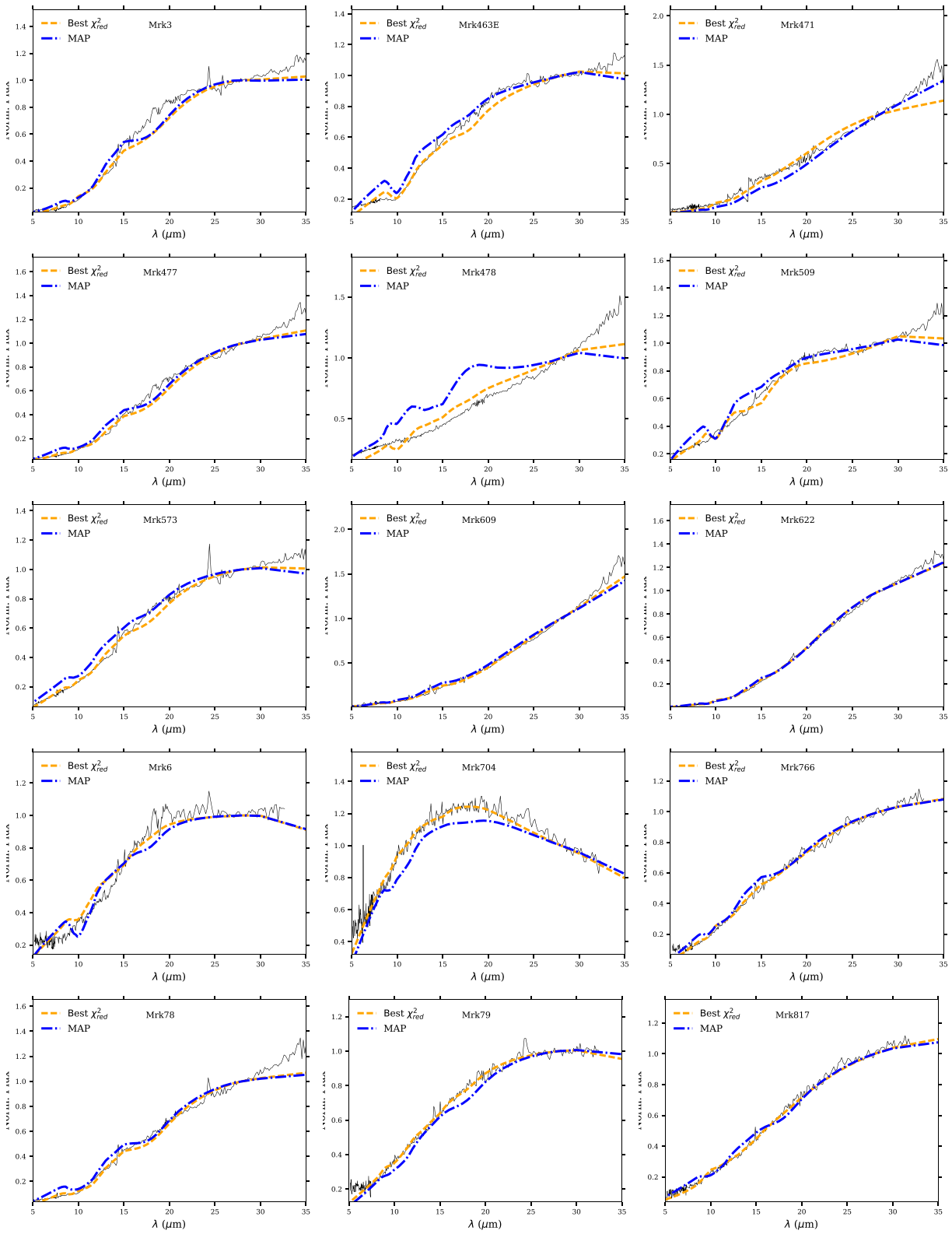

Figure C1 – *continued*

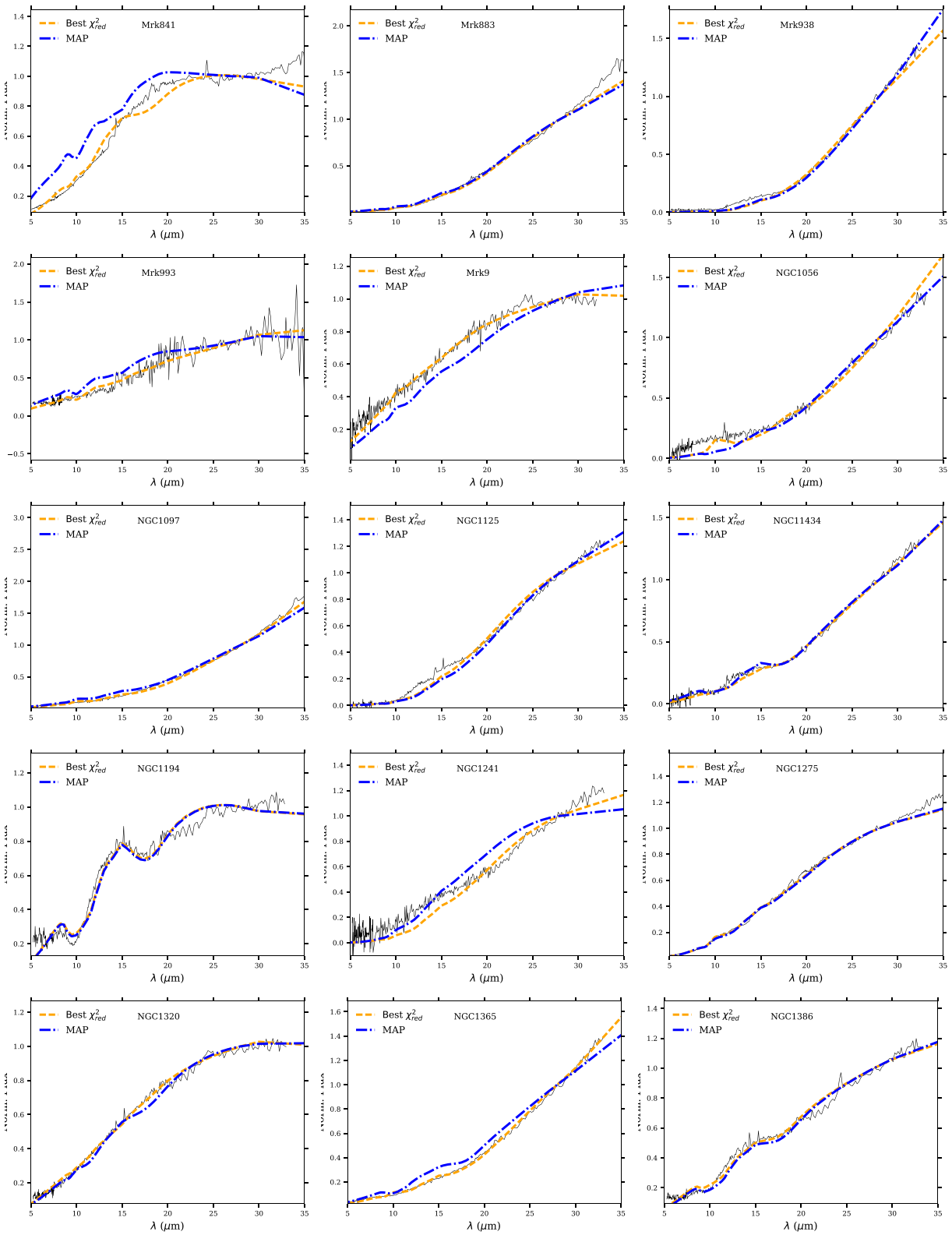

Figure C1 – *continued*

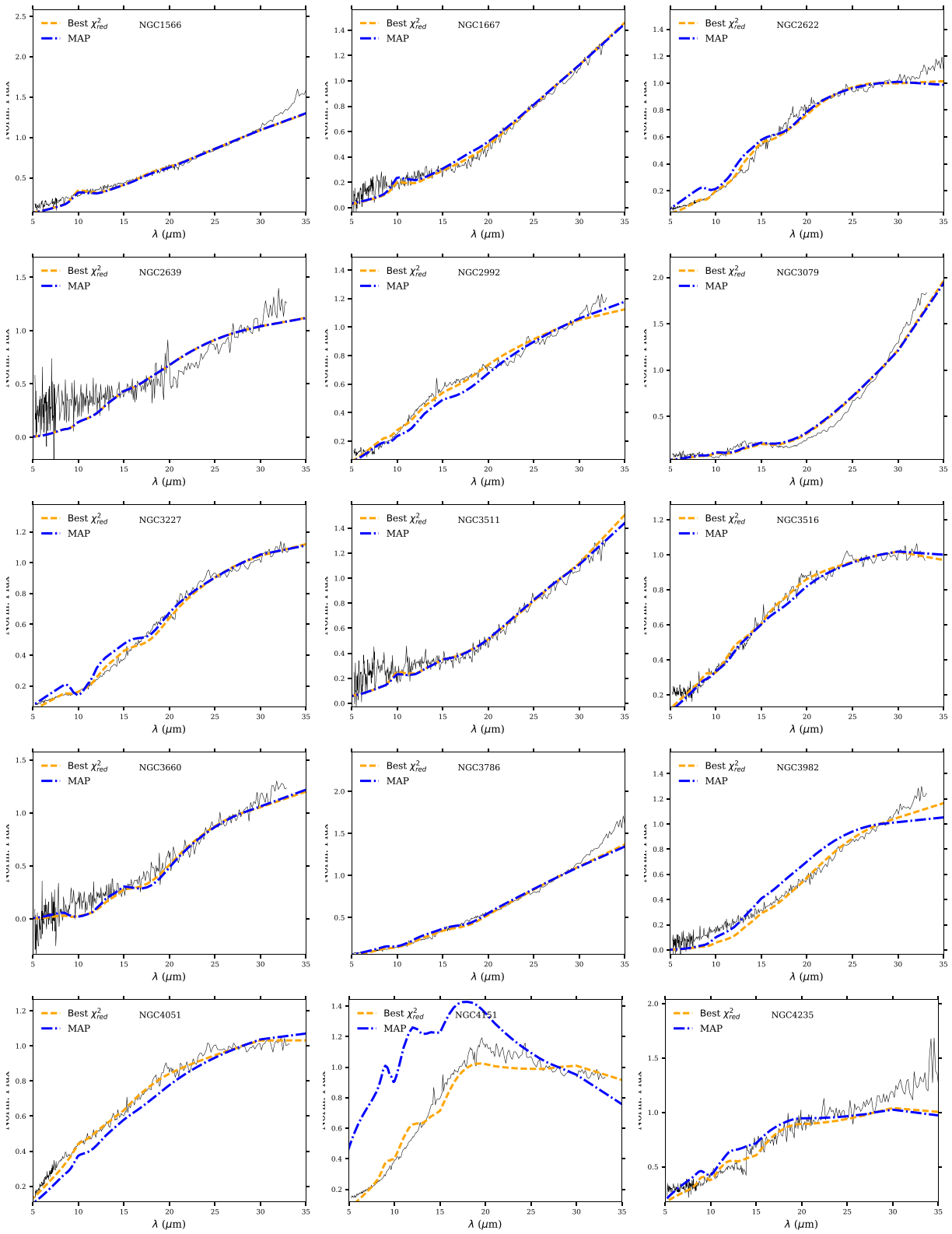

Figure C1 – *continued*

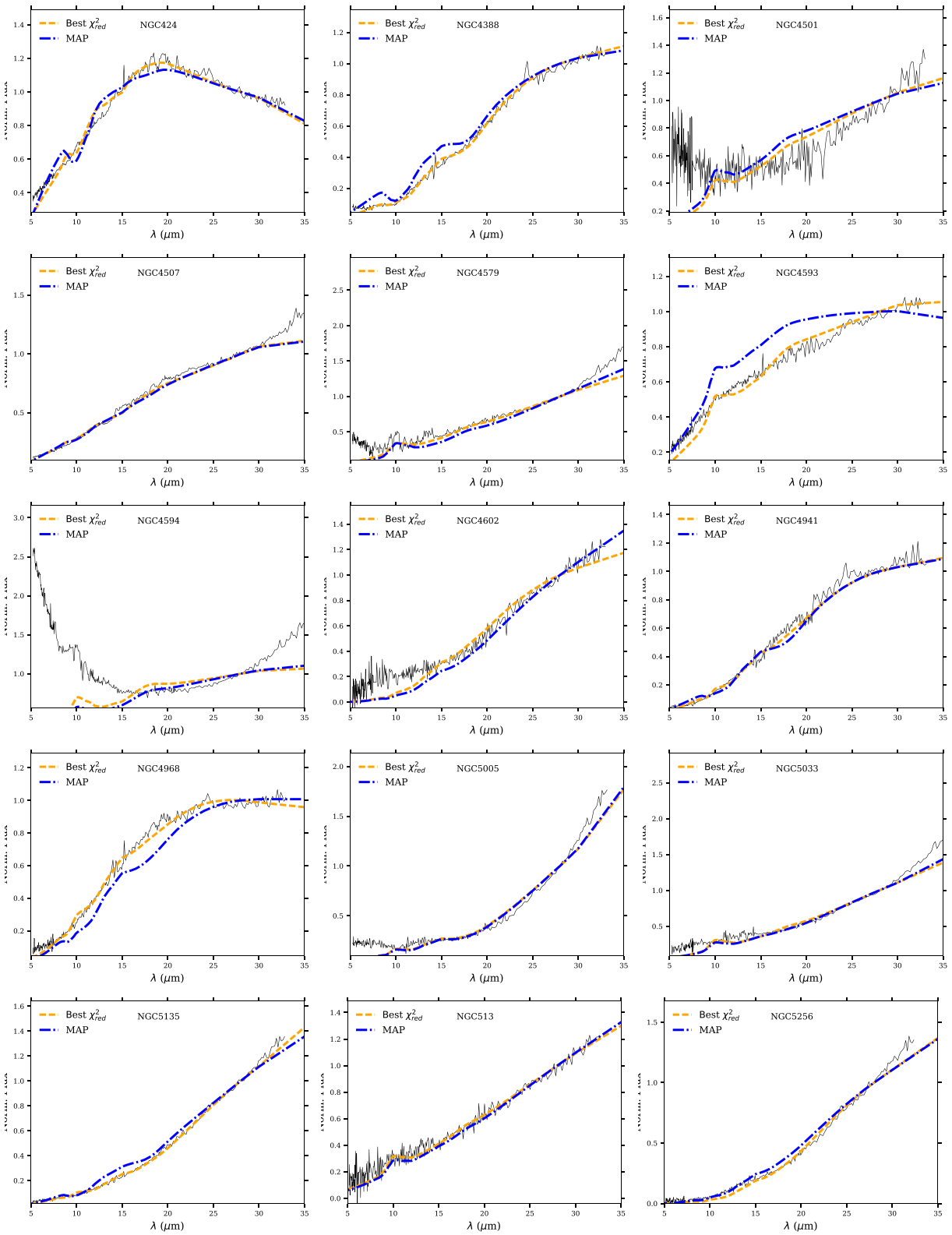

Figure C1 – *continued*

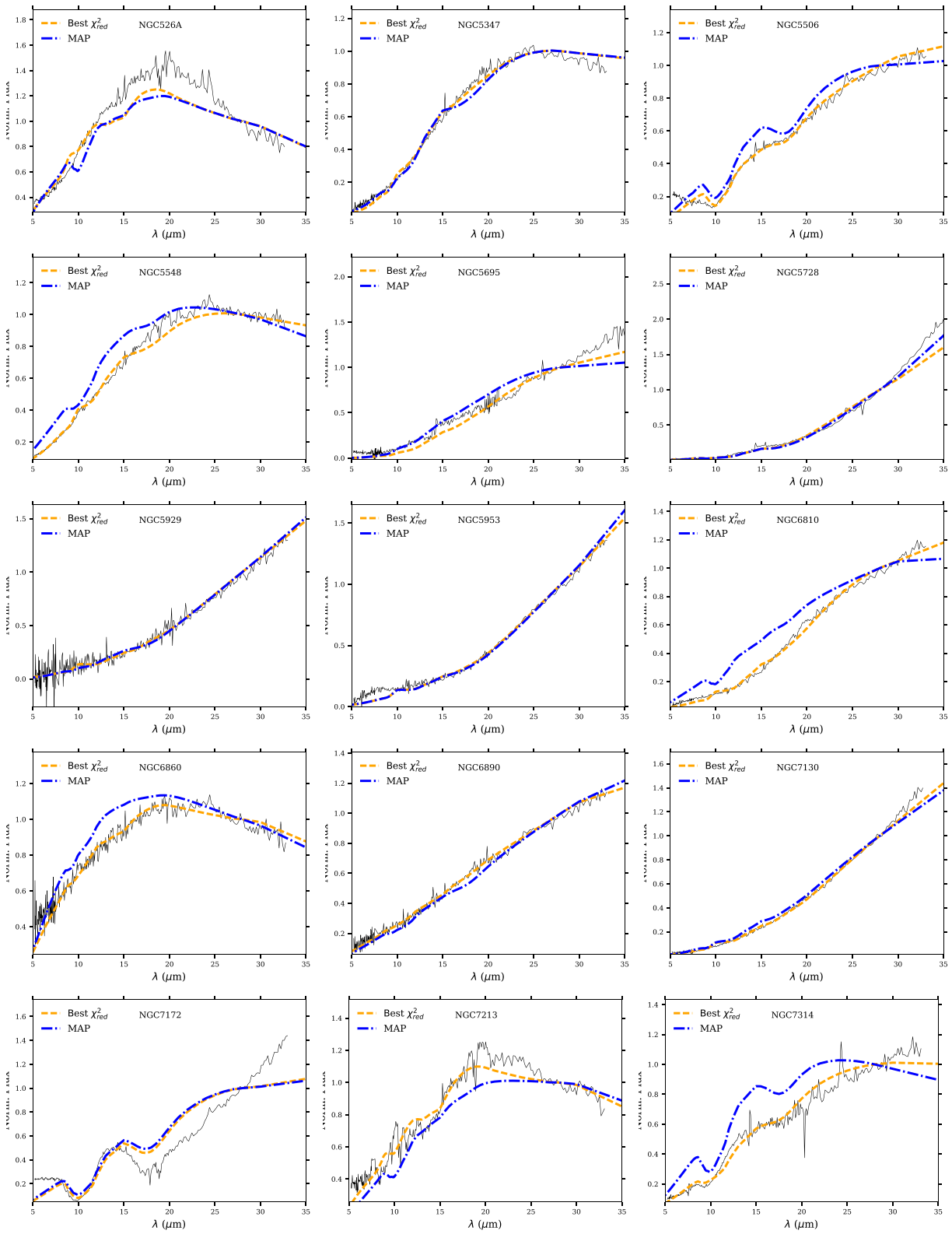

Figure C1 – *continued*

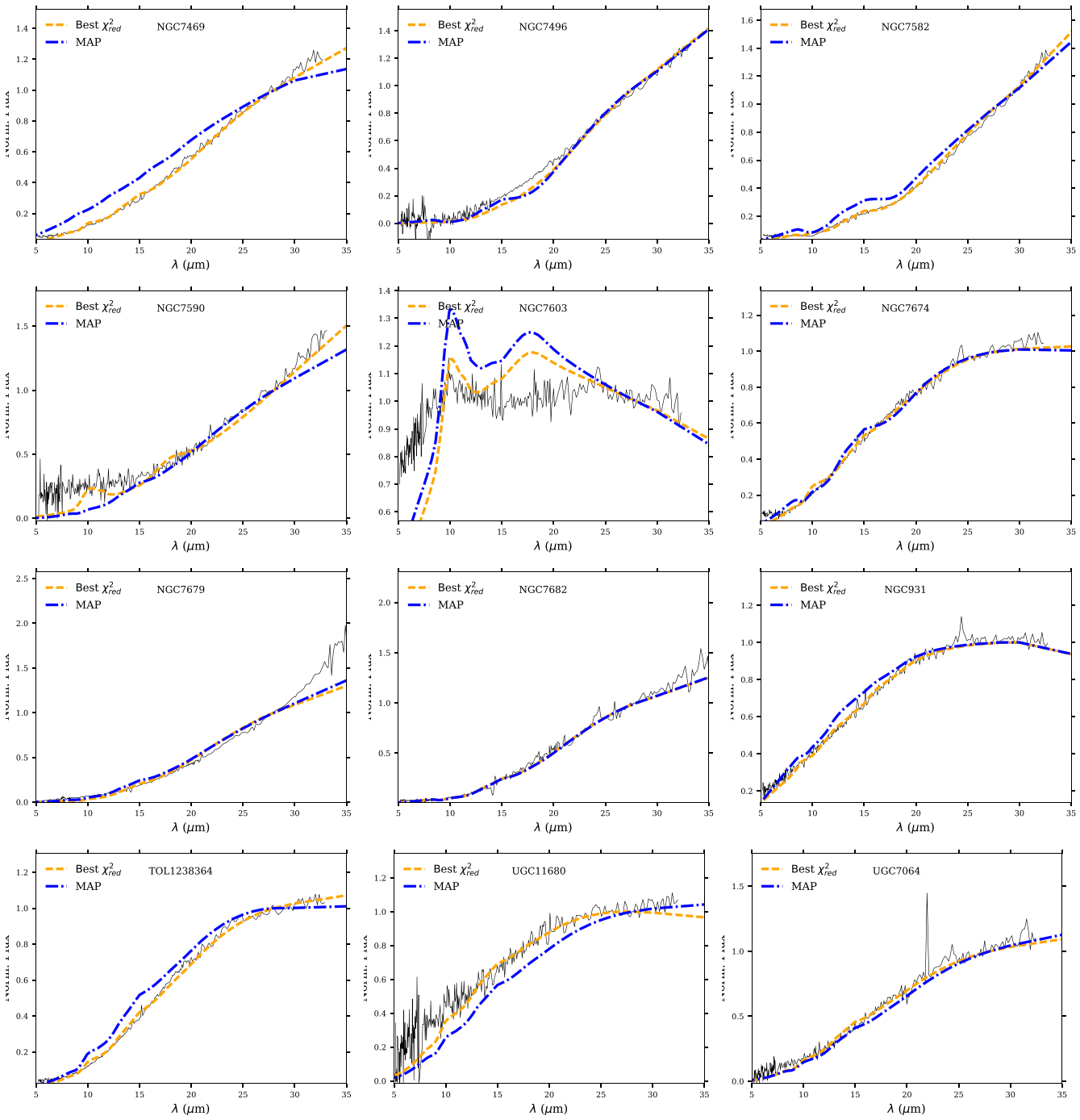

Figure C1 – *continued*

This paper has been typeset from a TEX/LATEX file prepared by the author.